



Australian Government
Bureau of Meteorology

The Centre for Australian Weather and Climate Research
A partnership between CSIRO and the Bureau of Meteorology

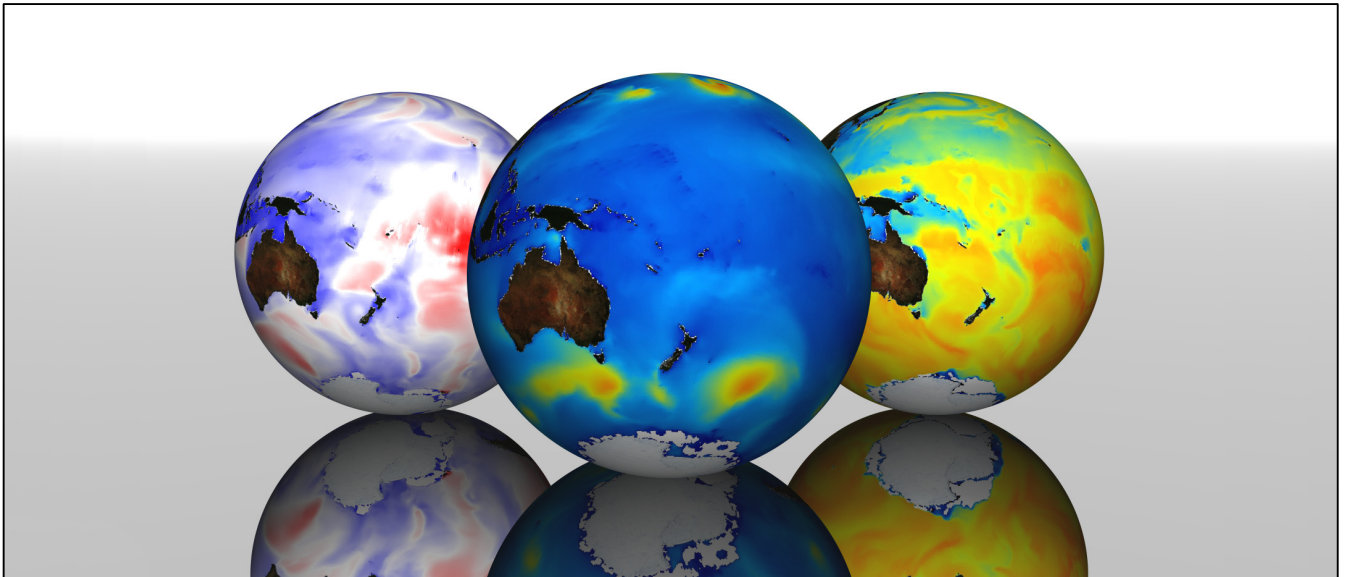


A Global Wave Hindcast focussed on the Central and South Pacific

Tom Durrant, Diana Greenslade, Mark Hemer and Claire Trenham

CAWCR Technical Report No. 070

April 2014



www.cawcr.gov.au



A Global Wave Hindcast focussed on the Central and South Pacific

Tom Durrant¹, Diana Greenslade¹, Mark Hemer² and Claire Trenham²

¹*Centre for Australian Weather and Climate Research
Bureau of Meteorology
GPO Box 1289, Melbourne, Vic 3001*

²*Centre for Australian Weather and Climate Research
CSIRO
GPO Box 1538, Hobart, Tas 7001*

CAWCR Technical Report No. 070

April 2014

ISSN: 1835-9884

National Library of Australia Cataloguing-in-Publication entry

Authors: Tom Durrant, Diana Greenslade, Mark Hemer and Claire Trenham
Title: A Global Wave Hindcast focussed on the Central and South Pacific
Edition: CAWCR Technical Report No. 070
ISBN: 9781486303175
Notes: Includes bibliographical references and index.
Subjects: Wind waves--Oceania--Mathematical models.
Marine meteorology--Oceania.
Pacific Area--Climate.
Islands of the Pacific--Climate.
Dewey Number: 551.4630996

Enquiries should be addressed to:
Dr Tom Durrant
Centre for Australian Weather and Climate Research
Bureau of Meteorology
GPO Box 1289
Melbourne, VIC 3001 Australia

Email: t.durrant@bom.gov.au
Ph. +61 9669 4813
Fax. +61 9669 4660

Acknowledgments

The Pacific-Australia Climate Change Science and Adaptation Planning Programme (PACCSAP) is funded by AusAID and The Department of Industry, Innovation, Climate Change, Science, Research and Tertiary Education (DIICCSRTE).

The Centre for Australian Weather and Climate Research (CAWCR), with which all authors of this report are affiliated, is a joint initiative between CSIRO and the Bureau of Meteorology.

Copyright and Disclaimer

© 2012 CSIRO and the Bureau of Meteorology. To the extent permitted by law, all rights are reserved and no part of this publication covered by copyright may be reproduced or copied in any form or by any means except with the written permission of CSIRO and the Bureau of Meteorology.

CSIRO and the Bureau of Meteorology advise that the information contained in this publication comprises general statements based on scientific research. The reader is advised and needs to be aware that such information may be incomplete or unable to be used in any specific situation. No reliance or actions must therefore be made on that information without seeking prior expert professional, scientific and technical advice. To the extent permitted by law, CSIRO and the Bureau of Meteorology (including each of its employees and consultants) excludes all liability to any person for any consequences, including but not limited to all losses, damages, costs, expenses and any other compensation, arising directly or indirectly from using this publication (in part or in whole) and any information or material contained in it.

All images reproduced in grayscale. A colour version of CAWCR Technical Report No.070 is available online: <http://www.cawcr.gov.au>

Contents

- 1. Introduction 1**
- 2. Previous work 2**
- 3. Model set-up 5**
 - 3.1 Grids 5
 - 3.2 Model settings 7
 - 3.3 Output data 9
 - 3.3.1 Gridded 9
 - 3.3.2 Spectral 10
- 4. Validation 11**
 - 4.1 Validation data sets 11
 - 4.2 Global validations 13
 - 4.2.1 Altimeters 13
 - 4.2.2 NDBC buoys 19
 - 4.3 South Pacific validations 23
 - 4.3.1 SOPAC buoys 23
- 5. Conclusions and outlook 27**
- References 29**
- Appendix A Model tuning 35**
- Appendix B Access details 37**
- Appendix C Additional altimeter validation results 39**
- Appendix D Additional NDBC validation results 42**
- Appendix E Additional SOPAC buoy validation results 45**

List of Figures

Fig. 1	Model grid resolutions used in the 31-year wave hindcast. High resolution grids are nested within a 0.4° global grid. Blue areas show regions of 10' resolution (~18km) and red areas indicate resolutions of 4' (~7km).	6
Fig. 2	Land sea mask for (a) the Southwest Pacific and (b) zoomed in over Fiji for the 1.5 degree ERA-40 grid, and the three grid resolutions used in this hindcast.	6
Fig. 3	Example of H_s (m) output for the global grid 0.4° grid (b) 10' and (c) 4' nested grids.....	9
Fig. 4	Spectral output points over the globe, and zoomed in over dense output area of the Australia and South Pacific.	10
Fig. 5	Time periods for which data is available from each altimeter.	11
Fig. 6	NDBC buoys used for validation	12
Fig. 7	SOPAC buoys used for model validation	12
Fig. 8	Time periods of available SOPAC buoy data in the South Pacific.....	13
Fig. 9	Example verification for 2005 H_s against altimeter data. Plots are (a) a QQ-plot (b) a PDF and (c) a scatter density plot.....	14
Fig. 10	Example verification for 2005 H_s against altimeter data. Plots show the global spatial distribution of (a) bias and (b) RMSE.....	15
Fig. 11	As Fig. 10, but with H_s (a) bias and (b) RMSE normalized by the mean observed value.	17
Fig. 12	Cumulative distribution of grid values from 3 x 3° gridded H_s statistics shown in Fig. 11 (a) for normalized bias and (b) normalised RMSE.....	17
Fig. 13	Monthly model error H_s statistics in reference to altimeter data.....	18
Fig. 14	Monthly mean (blue) and 80 th (pink), 90 th (cyan), 95 th (black) and 99 th (blue) percentile U_{10} (m s ⁻¹) for the entire CFSR dataset for the Northern Hemisphere (left) and Southern Hemisphere (right).....	19
Fig. 15	Model H_s bias (a) and RMSE (b) in meters for the entire hindcast relative to NDBC buoys.....	23
Fig. 16	(a) Bias and (b) RMSE of hindcast H_s from 4" grids against all available SOPAC. 25	
Fig. 17	Model grids and Google Earth TM images of SOPAC buoys (a) 41 - Fiji and (b) 33 - Tuvalu. Grids are shown with an example H_s field plotted. Black land is added by the plotting software for reference only, the model land-mask can be seen by white areas of missing data.	26
Fig. 18	H_s qq-plot, pdf, scatter density plot and time series plot of SOPAC buoys (a) 41 off Fiji and (b) 33 off Tuvalu.	27
Fig. 19	Global bias (m) on the left and global qq-plot on the right for modelled H_s compared to altimeter for the year of 2008 using default tunings for the Arduin 2010 source terms.	35
Fig. 20	Same as Fig. 19 but with reduced β_{max} from from 1.52 to 1.33.....	36
Fig. 21	Same as Fig. 20 but for model run with increased sheltering coefficient s_u from 1.0 to 1.2.....	36
Fig. 22	H_s bias relative to altimeter data for each year for the entire altimeter record.....	39
Fig. 23	QQ-plots, PDF's and scatter density plots of H_s calculated from model-altimeter co-locations separately for each year covered by the altimeter record.....	40

Fig. 24	Data availability for NDBC buoys used for verification.....	42
Fig. 25	Verification H_s plots for each all NDBC buoys. Plots are a quantile-quantile plot on the far left, distribution and density scatter plot	43
Fig. 26	H_s buoy/model QQ-plot, PDF, scatter density and time series plots for all available SOPAC buoy data	45

List of Tables

Table 1:	Details of available global reanalysis data sets.....	4
Table 2:	Grids used in the hindcast. See Fig.1 for graphical representation.	5
Table 3:	H_s statistics for the entire period against selected NDBC buoy observations.....	20
Table 4:	U_{10} statistics for the entire period against selected NDBC buoy observations.....	21
Table 5:	T_p statistics for the entire period against selected NDBC buoy observations	22
Table 6:	Statistics for H_s for the 4' grids against all available SOPAC observations and the Guam NDBC buoy (52200).....	24
Table 7:	Statistics for T_p for the 4' grids against all available SOPAC observations and the Guam NDBC buoy (52200).....	24
Table 8:	List of gridded variables available from hindcast.....	38

1. INTRODUCTION

Knowledge of historical wave conditions is necessary for many human endeavours, such as offshore structure design, coastal hazard assessment, and renewable energy applications to name a few. Surface driven wind-waves and their climatological variability must be considered within any comprehensive assessment of potential climate change-driven impacts on the coastal zone. For the island nations of the Central and South Pacific, these wave-driven impacts include: coastal flooding during storm wave events; coastal erosion, both during episodic storm events and due to long-term changes in wave climate; direct ecological impacts to reefs and subsequent morphological changes; flushing and circulation of lagoons and estuaries; and potential shipping and renewable wave energy solutions.

Studies of wave climate require datasets of sufficient duration and resolution, qualities that vary according to the specific application. Historical wave observations are primarily available from voluntary ships, moored buoys, and more recently, satellite altimetry. Ship observations give perhaps the longest record, however they are sparse, and of varying quality. Satellite altimeters provide excellent spatial coverage over the last few decades, but suffer from poor temporal coverage at any given location, and only provide a very limited number of observed variables. Despite these challenges, altimeter data have been used to great effect in several recent wave climate studies (e.g. Young 1999; Chen et al. 2002; Hemer et al. 2010; Young et al. 2011). Moored buoys provide the most comprehensive observing platform, however, these observations are few, located in selected areas generally along coastlines, and can only produce local wave estimates. Additionally, these data have historically come from the major North American and European buoy networks, with little buoy data available in the central and South Pacific.

Numerical wave models provide a valuable means of supplementing observations. Data from models have significant advantages over that from observing networks; most notably the ability to produce a consistent estimation of the wave field at high resolutions in both time and space, but also the ability to simulate a greater number of variables than can be reliably observed. Wave models have been run operationally for at least the last 20 years (a discussion of operational models from most major centres can be found in Bidlot et al. (2002) and Bidlot et al. (2007)), providing a useful source of wave data over that period. However, operational wave models are not stable over time, nor are the atmospheric models used to force them; as upgrades and changes occur, inhomogeneities in the historical data sets are introduced.

As such, it is useful to periodically re-run a model over a defined historical period using the current models, providing an historical data set that is of state-of-the-art quality, as well as being consistent through time. In the case of atmospheric models, constraining the model through the assimilation of observations is a critical component of the initial value problem being solved. The production of so called reanalysis datasets is, as such, no small undertaking, a significant component of which is the collection and quality control of large amounts of observational data (e.g. Kalnay & Kanamitsu 1996; Kanamitsu et al. 2002; Saha et al. 2010; Dee et al. 2011). The assimilation of observations in historical wave

model runs is less critical; waves present a forced damped problem, rather than an initial value problem, with the dominant forcing coming from the surface winds. It is also less practical: wave observations are relatively sparse in space and time compared to those going into an atmospheric reanalysis. In the absence of any assimilation of observations, the term wave hindcast is often applied to historical wave simulations.

Existing wave hindcasts and reanalyses in the Pacific region were examined by Hemer et al. (2011) and found to be too coarse both spatially and temporally to adequately capture the complex wave environment in the Pacific region, highlighting the need for a high-resolution hindcast. The ability to produce such a hindcast has historically been limited by the lack of a global high-resolution reanalysis wind product with which to force the wave model. The recently completed Climate Forecast System Reanalysis (CFSR; Saha et al., 2010), provides hourly surface winds on a 0.3° by 0.3° latitude-longitude spatial grid, creating an opportunity to produce a significantly higher resolution wave hindcast than has previously been possible.

This report describes a 31-year wave hindcast covering the period 1979 to 2009. This hindcast provides wave data over the globe hourly at 0.4° , making it significantly higher resolution than previously available global data sets. Additionally, a series of nested grids provides very high-resolution data in the South Pacific and around the Australian coastline. The report is structured as follows: some previous work is outlined in Section 2, the model set up is described in Section 3, validation against observations is presented in Section 4 and finally conclusions and an outlook are given in Section 5.

This work comprises one part of a two part contribution to the Pacific-Australia Climate Change Science and Adaptation Planning (PACCSAP) Program, examining future climate in the South Pacific¹. In addition to examining current wave climate in the region, as enabled by the high resolution global and regional wave hindcast presented here, climate model-driven projections of possible future wave climate have also been examined by Trenham et al. (2013).

2. PREVIOUS WORK

A number of wave hindcasts and wave reanalyses have been previously conducted. A review of the available hindcast data in the Pacific was conducted by Hemer et al. (2011). They concluded that the most suitable data set available at the time was the ERA-Interim reanalysis. The ERA-Interim reanalysis followed on from the longer ERA-40 reanalysis. The European Centre for Medium-Range Weather Forecasts (ECMWF) completed the ERA-40 reanalysis of global meteorological variables, including surface waves, using ECMWF's integrated forecasting system, a coupled atmosphere-wave model that uses variational data assimilation (Uppala et al. 2005). The period of the reanalysis was from September 1957 to August 2002 (45 years), and includes ocean surface wind waves on a $1.5^\circ \times 1.5^\circ$ latitude-longitude grid covering the whole globe, generated using ECMWF's coupled WAM wave model (Janssen et al. 1994). Caires & Sterl (2005) carried out an

¹ <http://www.pacificclimatechangescience.org/>

extensive assessment of the quality of the significant wave height (H_s) and mean wave period (T_m) produced from the reanalysis, comparing the data against 20 United States National Data Buoy Centre (NDBC) waverider buoys, and “along-track quality” checked deep-water altimeter measurements of H_s from the satellite platforms GEOSAT, TOPEX, ERS-1 and ERS-2. ERA-Interim is a reanalysis similar to ERA-40, where the ECMWF integrated forecasting system was used to describe the state of the atmosphere, land and ocean-wave conditions (Dee et al. 2011). ERA-Interim was intended as an Interim reanalysis in preparation for the next generation extended reanalysis (ERA-clim) which will replace ERA-40. ERA-Interim data is available at a higher spatial resolution (0.7° globally) than ERA-40, and though originally covered only 1989 to 2010, it has recently been extended back to 1979. ERA-Interim surface wave data which are freely available to the research community include 6-hourly values of H_s , T_m and mean wave direction (D_m) at 1.5° spatial resolution.

These hindcasts and reanalyses contain several shortcomings from the perspective of useful data in the South Pacific. The most obvious is resolution. Coarse spatial resolution influences two aspects of the wave climate: 1) the coarse model resolution results in reduced intensity of strong storm systems (e.g., tropical cyclones), and waves resulting from these events are likely to be significantly underestimated; and 2) the resolution is coarse with respect to individual islands, and so only the broad scale wave properties in the region may be determined. Furthermore, the available outputs are limited. ERA-Interim only outputs H_s , T_m and D_m . These are not sufficient to distinguish between locally-generated wind sea, and swell generated by storms elsewhere and propagating to the site, which is potentially of great importance for studying wave induced inundation in the region (Hoeke et. al. 2013). Ideally, full spectral information would be available, both as a research resource, and also to provide adequate boundary conditions for further coastal impact modelling studies.

Historically, the limitation on the resolution of wave hindcasts has not directly been a computational constraint, but rather the availability of suitable resolution winds. With the exception of the ECWMF reanalysis, which explicitly couples the waves and atmosphere, the resolution of wave hindcasts has been practically constrained by the spatial and temporal resolution of available winds, limiting the ability to accurately capture the wave field (see Table 1 for resolution of surface wind fields from available atmospheric reanalyses).

Table 1: Details of available global reanalysis data sets

Name	Source	Period Covered	Highest Available Spatial Resolution	Temporal Resolution
ECMWF 40 year Reanalysis (ERA-40)	ECMWF	1958-2001	1.25° x 1.25°	6 hourly
ECMWF Interim Reanalysis (ERA-Interim)	ECMWF	1979-Present	0.75 x 0.75	3 hourly
Japanese Reanalysis (JRA-25)	Japan Meteorological Agency	1979-Present	1.25° x 1.25°	6 hourly
NCEP/NCAR Reanalysis I (R1)	NCEP	1979-Present	2.5° x 2.5°	6 hourly
NCEP/DOE Reanalysis AMIP-II (R2)	NCEP/DOE	1979-Present	2.5° x 2.5°	3 hourly
NCEP Climate Forecast System Reanalysis (CFSR)	NCEP/NCAR	1979-Present	0.3° x 0.3°	Hourly
NASA MERRA	NASA	1979-2009	$2/3^\circ$ lon x $1/2^\circ$ lat	Hourly

This shortcoming has been addressed by the recently completed CFSR data set (Saha et al., 2010), produced by the National Centers for Environmental Prediction (NCEP). This reanalysis supersedes the widely used NCEP/DOE reanalysis (R1: Kalnay & Kanamitsu 1996) and NCEP/NCAR Reanalysis II (R2: Kanamitsu et al. 2002). Improvements include significant upgrades in resolution, spatial resolution has increased from 2.5° to 0.3° horizontally and the number of vertical levels increased from 28 to 64, output frequency increased from 6 hourly to hourly; dynamical improvements, the atmospheric model is now coupled to an ocean circulation model and an interactive sea ice model; and improvements to the data assimilation scheme, both in terms of the sophistication of the methods employed and the volume and quality of the observations ingested. This reanalysis presents a compelling opportunity for the purposes of wave hindcasting.

There have been several parallel efforts to utilise these data in the production of wave hindcasts. Chawla et al. (2012) performed a 30 year hindcast on a 0.5 degree global grid, with a number of higher resolution nested grids around the U.S, European and Australian coasts, as well as the U.S. Territories in the Pacific. Similarly, Rasche & Arduin (2013) have produced a similar global hindcast at 0.5 degree, with nested grids concentrating on the European coast, as well as French territories in the Pacific covering the period. The hindcast presented here differs from these two in several ways, this will be discussed in Section 3.2. The primary point of difference is that this work focuses specifically on the South and Central Pacific and Australia, with high spatial and temporal resolution in this region being paramount.

3. MODEL SET-UP

3.1 Grids

The hindcast was performed using the WAVEWATCH IIITM model version 4.08 (Tolman 1991; Tolman 2009). A series of nested grids was run within a global grid, following the so-called mosaic grid approach of Tolman (2008). This framework enables a series of overlapping grids of different resolutions to be run simultaneously, with fine scale grids receiving information from coarse grids, and the added detail achievable in fine grids being fed back to the coarse large scale grids, enabling the model resolution to be locally increased in a way that maintains consistency between grids. These grids need not be rectangular, allowing grids to conform to coastlines, reducing computational expense in the open ocean where the benefits of higher resolution are less.

Five grids were used; a $0.4^\circ \times 0.4^\circ$ global grid and two sets of two nested grids of $10'$ ($\sim 18\text{km}$) down to $4'$ ($\sim 7\text{km}$) around the Australian coast and in the South Pacific. Details of geographical extents are given in Table 2 and shown graphically in Fig. 1. All grids are run for the entire hindcast period from 1979 to 2009.

Table 2: Grids used in the hindcast. See Fig.1 for graphical representation.

Grid Name	Geographical Extent (lat range, lon range)	Spatial Resolution
glob_24m	0-359.6; -78-78	0.4° ($\sim 50\text{km}$)
aus_10m	100.0-175.0, -50.0-3.0	$10'$ ($\sim 18\text{km}$)
aus_4m	100.0-175.0, -50.0-3.0	$4'$ ($\sim 4\text{km}$)
pac_10m	125.0-210.0, -30.0-20.0	$10'$ ($\sim 18\text{km}$)
pac_4m	125.0-210.0, -30.0-20.0	$4'$ ($\sim 4\text{km}$)

The detail achievable in these grids can be seen in Fig. 2 showing the land sea mask for a large part of the South Pacific (a), and zoomed in over Fiji (b) for each of these resolutions, as well as the resolution of the ERA-40 dataset for comparison. In the case of the 1.5° grid, resolution is clearly inadequate to capture the complex bathymetry of the region, with Fiji not resolved at all. The 0.4° grid offers significant improvement, but the complexity of the region is apparent by the added detail captured in the 18km and 7km grids.

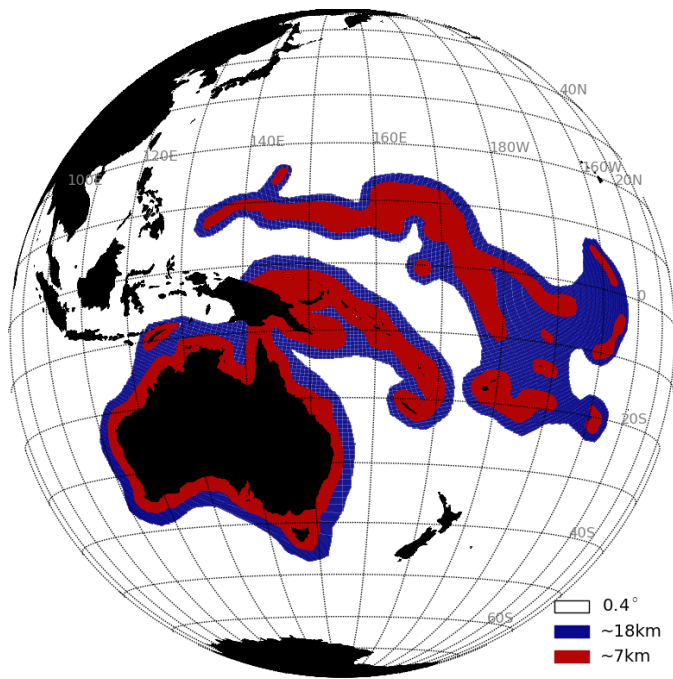


Fig. 1 Model grid resolutions used in the 31-year wave hindcast. High resolution grids are nested within a 0.4° global grid. Blue areas show regions of 10' resolution (~18km) and red areas indicate resolutions of 4' (~7km).

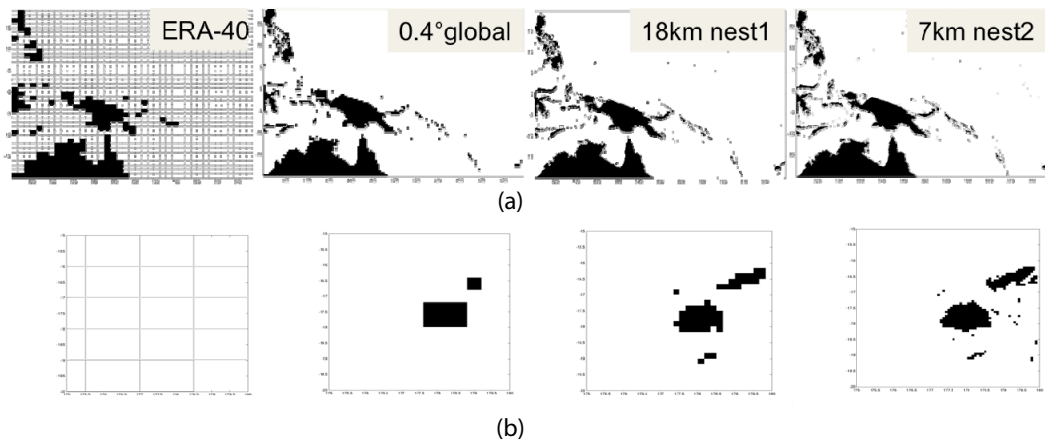


Fig. 2 Land sea mask for (a) the Southwest Pacific and (b) zoomed in over Fiji for the 1.5 degree ERA-40 grid, and the three grid resolutions used in this hindcast.

Of significant relevance for modeling in the Pacific, WAVEWATCH III can account for blocking of wave energy by obstacles, such as small islands, that are too small to be explicitly resolved at the given resolution of a grid (Tolman 2003). Neglecting to take account of this is well known to result in large positive biases in the Pacific in particular (Tolman 2003). All the grids used here were constructed using the DBDB2v3 digital bathymetric dataset (NRL 2006), with a resolution of 2' and refined with the Global Self-consistent Hierarchical High resolution Shoreline (GSHHS) database following Chawla & Tolman (2008). The use of the GSHHS database enables small islands and structures to be

resolved that are beyond the capability of the bathymetry. The wave spectra were discretized over 29 frequencies exponentially spaced from 0.038 Hz to 0.5 Hz and 24 directions with a constant 15° directional resolution.

All grids were forced with surface winds (10 m winds: U_{10}) from CFSR data at 0.3° spatial and hourly temporal resolution. Six-hourly sea ice concentrations from CFSR were also used with the continuous ice treatment method of Tolman (2003) employed, with default threshold concentrations of 0.25 for the ice to have no effect on propagation, 0.75 for ice to be treated as land, and increasing levels of blocking applied for concentrations between these values (as described in Tolman (2003)).

3.2 Model settings

Spectral wave modelling is based on the decomposition of the surface elevation variance across wave numbers k and directions θ . The development of the spectral density function $F(k, \theta)$ in space and time is governed by the wave transport or energy balance equation:

$$\frac{DF}{Dt} = S_{tot} \quad (1)$$

Non-conservative sources and sinks of wave energy on the right-hand-side of Equation 1 consist, in deep water, of the input of wave energy by wind (S_{in}), nonlinear interactions between waves (S_{nl}) and dissipation due to wave breaking or ‘white-capping’ (S_{ds}). A number of additional terms may be applied in shallow water, bottom friction and surf breaking and depth induced breaking are applied here, as detailed below.

WAVEWATCH III contains a number of physics options. The choices made here were on the basis of hindcast validation during a selected year: 2008 (see Appendix A). Some brief descriptions are given below:

1. The source terms used are the parameterizations of Ardhuin et al. (2010).
2. The Discrete Interaction Approximation (DIA: Hasselmann et al. 1985) is used for computation of the non-linear wave-wave interactions.
3. JONSWAP bottom friction (Hasselmann et al. 1973) is used.
4. Battjes & Janssen (1978) shallow water depth breaking is activated with a Miche-style shallow water limiter for maximum energy.
5. Third order Ultimate Quickest propagation scheme is used (Leonard 1979; Leonard 1991) including the correction for spurious effects of spectral discretization (the garden sprinkler effect), as proposed by Tolman (2002a).

A detailed description of all of these model components is outside the scope of this document, and the interested reader is referred to the papers listed. However, a short qualitative description of novel features of the Ardhuin et al. (2010) source terms follows with the intention of placing this hindcast in context to those discussed in Section 2.

Until recently, two source term packages have been most widely used. The first is WAM Cycle 4, consisting of the input term of Janssen (1991) and a dissipation term based on Komen et al. (1984) with adjustments of Bidlot et al. (2005) (hereafter referred to as the BJA terms). These are the terms used operationally at ECMWF and those used in the ERA-Interim reanalysis. The second are those of Tolman & Chalikov (1996, hereafter TC96). The wind input source term is based on numerical predictions of air flow over waves (Chalikov & Belevich 1993; Chalikov 1995). Dissipation is handled with two distinct formulations employed at high and low frequencies, allowing the separation of the physical processes contributing to dissipation at these respective scales. Unlike WAM variant terms, swell dissipation is explicitly accounted for in the TC96 terms, in the form of a negative wind input for waves traveling faster than, or at large angles to the wind. The importance of swell dissipation on global scales was determined heuristically in this case by Tolman (2002b). These terms were used operationally at NCEP until recently, and are used in the recent hindcast of Chawla et al. (2012).

The Ardhuin et al. (2010) terms consist of a modified wind input term based on Janssen (1991), and a new dissipation term. Novel features of these terms include:

- Separate accounting of swell dissipation due to negative wind input from that due to breaking, following Tolman & Chalikov (1996).
- A non-linear swell dissipation based on observed dissipation rates across the Pacific observed from SAR data (Ardhuin et al. 2009).
- A breaking induced dissipation based on the local saturation spectrum rather than the total mean slope (addressing issues with the previous WAM dissipation of Komen et al. (1984)).
- A cumulative dissipation rate following Young & Babanin (2006).
- A reduced wind input at high frequencies compared to Janssen (1991), and an intermediate input level at the peak, compared to the higher values with Janssen (1991) and much lower values with Tolman & Chalikov (1996). This effect is parameterized as a sheltering term, reducing the effective winds for the shorter waves (e.g. Chen & Belcher 2000; Banner & Morison 2010).

These terms are used operationally by the French Navy (Naval Hydrographic and Oceanographic Service, SHOM (Ardhuin, 2010)) and have recently replaced the TC96 terms in the NOAA operational model².

The skill of modern wave models is such that the quality of the wave field is critically dependent on the quality of forcing winds (e.g. Cardone et al. 1996; Rogers & Wittmann 2002). The atmospheric models used to both develop, and operationally run wave models have characteristic biases that differ from one model to another (e.g. Chelton & Freilich 2005; Durrant & Greenslade 2012) to which the wave model is highly sensitive (Durrant et al. 2013). Though the quality of the CFSR winds has been shown to be very good (e.g. Cox et al. 2011), some tuning of the source terms is necessary to achieve optimal results.

² http://www.nws.noaa.gov/om/notification/tin12-17wave_physics.htm

In the case of the source terms of Ardhuin et al. (2010) used here, some recommended tunings for CFSR winds are present in the WAVEWATCH III manual (TEST451f), and these tunings were largely adopted. During the 2008 verification period, it was found that the recommended tunings produced a positive bias in the mid-latitude storm belts. This was reduced by slightly increasing the strength of the sheltering term discussed above, effectively reducing the high frequency input in the wind input term for strong winds. Full details can be found in Appendix A.

3.3 Output data

3.3.1 Gridded

Gridded outputs include commonly used variables such as H_s , T_p , T_m and so on, as well as many other wave related parameters such as partitioned wave details, stresses, Stokes drift etc. Each variable is available hourly for each grid, at the native resolution, for the full 31 years. An example of the H_s field for each grid is shown in Fig. 3. The full list of variables is given in Appendix B.

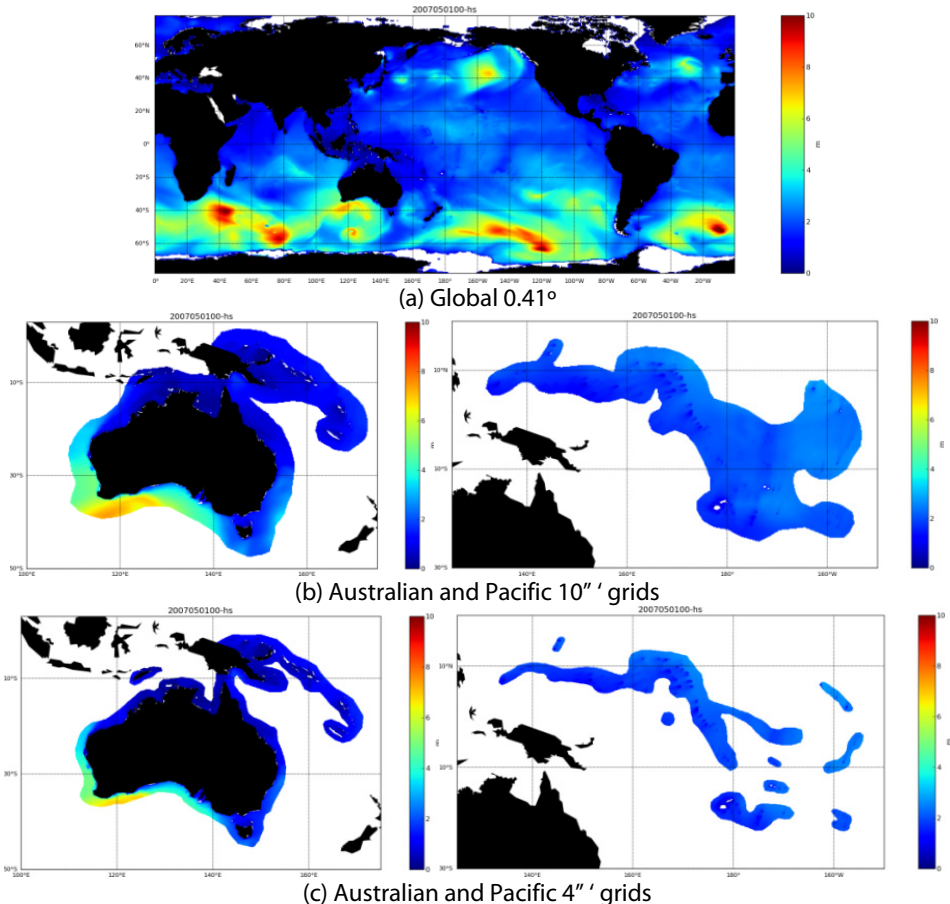


Fig. 3 Example of H_s (m) output for the global grid 0.4° grid (b) 10' and (c) 4' nested grids.

3.3.2 Spectral

Spectral data at a large number of points (~3600) have been output, providing the full wave spectrum at hourly intervals. These locations include buoy sites, various points of specific interest, and at regular spacing of 0.5° within the $4'$ grids, and 10° in the global grid. These points are shown in Fig. 4. Spectral data is given in the native spectral resolution that the model is run, i.e. 29 frequencies exponentially spaced from 0.038 Hz to 0.5 Hz and 24 directions with a constant 15° directional resolution. This high density of output points in the South Pacific and around the Australian coast provides valuable data for regional wave studies, as well as a versatile source of boundary data for higher resolution coastal impact studies.

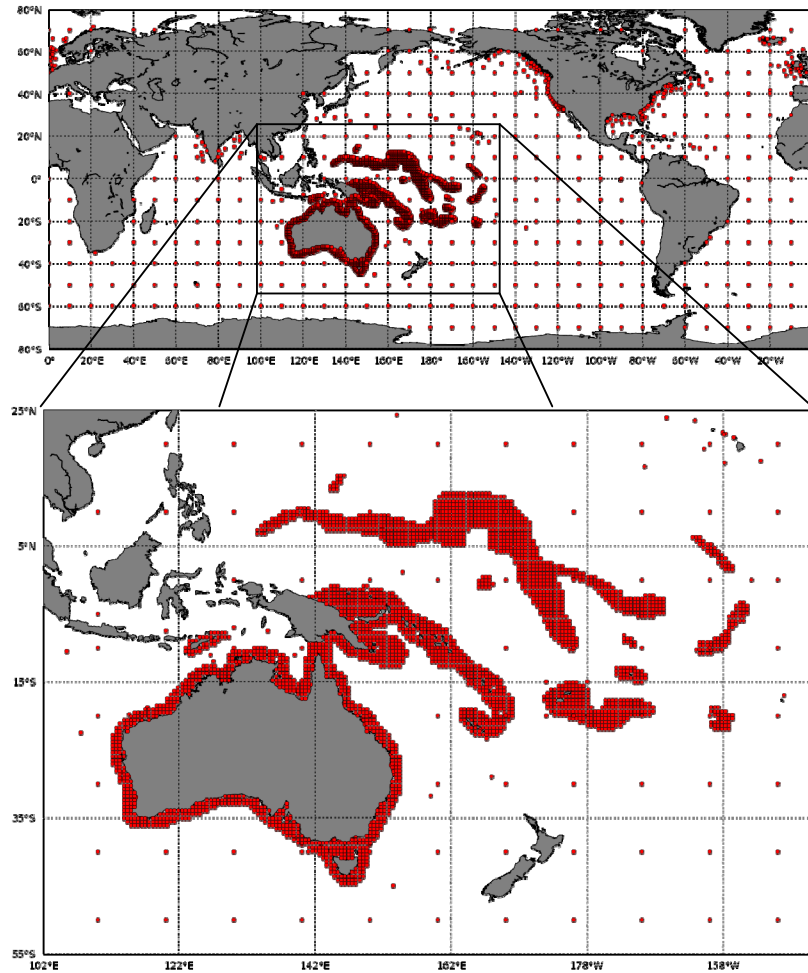


Fig. 4 Spectral output points over the globe, and zoomed in over dense output area of the Australia and South Pacific.

Details of data access are given in Appendix B.

4. VALIDATION

4.1 Validation data sets

Validation has been carried out using both remotely sensed satellite altimeter observations, and *in-situ* buoy measurements. Altimeter data error variances are comparable to those of buoy data (Caires & Sterl 2003). They do, however, typically contain systematic biases (e.g. Cotton & Carter 1994; Durrant et al. 2009) that must be removed, especially when considering multiple instruments over a long period, as is the case here. Data used here were obtained from the quality controlled, calibrated and homogenised data set maintained at the French Research Institute for Exploitation of the Sea (IFREMER) (Queffeuou & Croizé-fillon 2012). A total of eight altimeters are considered here, GEOSAT from 1985 through to 1989, then continuous coverage from 1993 through to 2010 with ERS-1, TOPEX, ERS-2, GFO, JASON-1, ENVISAT and JASON-2. Temporal coverage of each instrument is shown in Fig. 5.

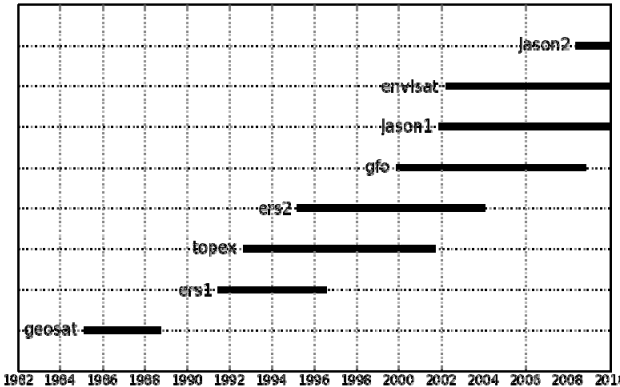


Fig. 5 Time periods for which data is available from each altimeter.

For the global grid, buoy validations are carried out using the historical buoy data archive from NDBC. These buoys provide an excellent quality controlled data set covering the entire period of the hindcast. A selection of buoys is chosen here that have long historical records. In addition, the Guam (52200) buoy provides valuable data in the Pacific from 2004 onwards. The NDBC buoys considered are shown in Fig. 6.

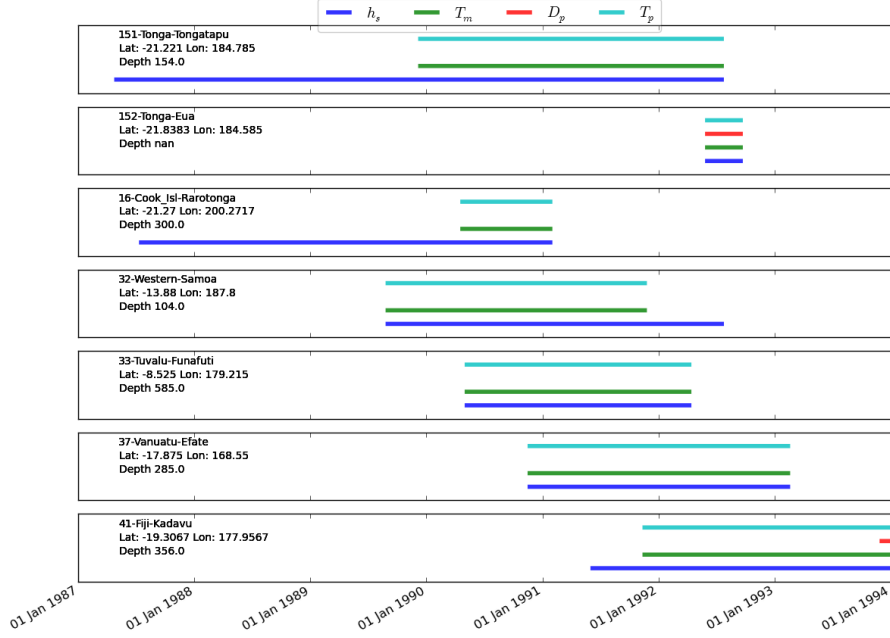


Fig. 8 Time periods of available SOPAC buoy data in the South Pacific

4.2 Global validations

4.2.1 Altimeters

In order to undertake model-observation comparisons, model data is bi-linearly interpolated in space and linearly interpolated in time to make up a set of co-locations from which various statistics are calculated. Statistics used here are bias, root-mean-square-error (RMSE), scatter index (SI) and Pearson correlation coefficient (R), as defined in follows:

$$Bias = \frac{1}{N} \sum_{i=1}^N (M_i - O_i) \quad (3)$$

$$RMSE = \sqrt{\frac{1}{N} \sum_{i=1}^N (M_i - O_i)^2} \quad (4)$$

$$SI = \sqrt{\frac{\frac{1}{N} \sum_{i=1}^N ((M_i - \bar{M}) - (O_i - \bar{O}))^2}{\bar{O}}} \quad (5)$$

$$R = \frac{\sum_{i=1}^N (M_i - \bar{M})(O_i - \bar{O})}{\sqrt{\sum_{i=1}^N (M_i - \bar{M})^2 (O_i - \bar{O})^2}} \quad (6)$$

where M_i is the model value, O_i is the observed value, N is the number of co-locations and an overbar represents the mean value.

Results for the full year of 2005 are presented here; H_s statistics and validation plots for all years of available data are presented in Appendix C. Figure 9 shows a quantile-quantile plot (QQ-plot), probability density function (PDF) and scatter density plot constructed from co-locations from all available altimeter observations for the year 2005 (GFO, Envisat and Jason-1). Note that here, and throughout this report; black dots in the QQ-plot indicate 0-99th percentiles, while the red show the 99-99.9th percentile; scatter density plots are shown on a log scale. These results indicate excellent agreement between the model and altimeter observations. RMSE is around 37 cm and SI is around 13%. Agreement is good throughout the wave range, with PDFs for observations and model values showing very similar shapes, and QQ-plots indicating excellent agreement all the way up to the 99.9th percentile.

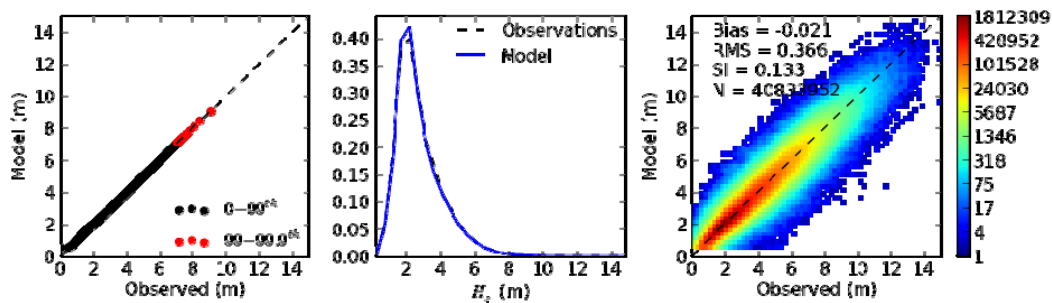


Fig. 9 Example verification for 2005 H_s against altimeter data. Plots are (a) a QQ-plot (b) a PDF and (c) a scatter density plot.

Figure 10 shows these same co-locations used to construct spatial distributions of H_s (a) bias and (b) RMSE over the globe, with statistics calculated here on a $3 \times 3^\circ$ grid. RMSE values are less than 50 cm over most of the globe, and typically around 20 cm in the Tropics. Some regional biases are apparent, though these are relatively slight. Of particular note:

- The signature positive biases in the eastern edges of the major ocean basins seen in the BJA terms (e.g. Tolman 2002b; Rogers & Wittmann 2002; Collard et al. 2009; Durrant et al. 2012) have been eliminated, due to explicit inclusion of swell dissipation (Ardhuin, 2010).
- The positive bias in the Southern Ocean in the terms of TC96 (e.g. Chawla et al. 2009; Chawla et al. 2012)) and to a lesser extent the BJA terms (e.g. Bender 1996; Cavaleri 2009) has been greatly reduced.

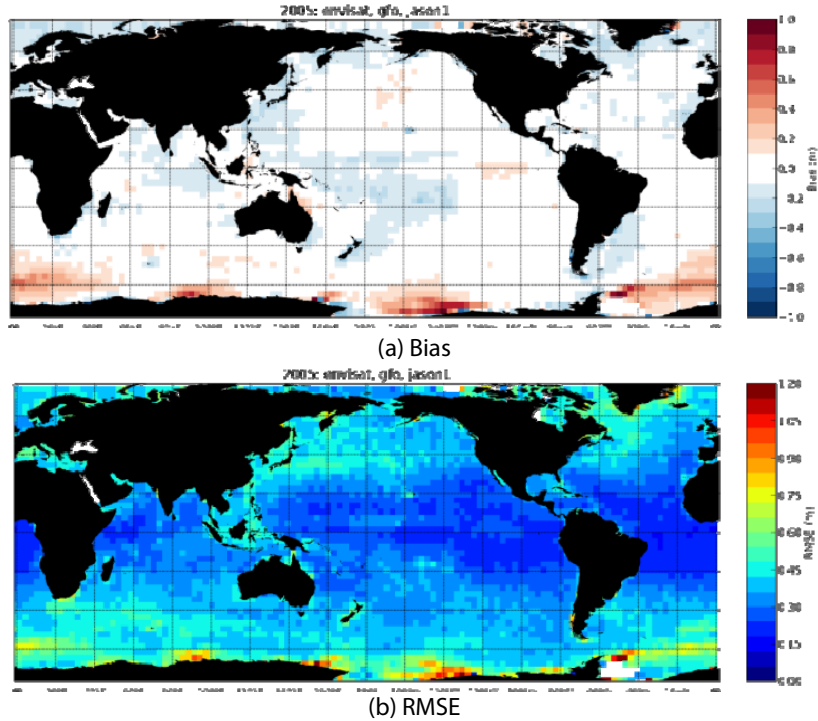


Fig. 10 Example verification for 2005 H_s against altimeter data. Plots show the global spatial distribution of (a) bias and (b) RMSE

Several undesirable features are, however, apparent:

- Areas of positive bias are evident around the Antarctic. A convincing explanation for this has been put forward by Ardhuin et al. (2011). The calving of icebergs into the Southern Ocean around the ice edge collectively creates significant blocking of wave energy, a process that is not explicitly accounted for here. By including this effect in the form of a temporally varying sub-grid-scale blocking grid in WAVEWATCH III, constructed based on icebergs identified using noise in altimeter observations, Ardhuin et al. (2011) have demonstrated that this bias can be greatly reduced.
- A slight negative bias is apparent in the western tropical Pacific. This may be due to the lack of any shoreline reflection. WAVEWATCH III currently does not include this, with all incident wave energy removed at land boundaries. For most natural beaches, reflection is generally weak, typically of the scale of 5% of incoming energy (e.g. Elgar et al. 1994), making it generally of little relevance on the scales considered here. However, in the case of steep shoreline profiles, such as those of the volcanic islands in the South Pacific, the amount of reflected energy can be substantially greater. This, coupled with the large number of islands in the South Pacific could make the neglect of this physical process locally significant. Indeed recent work by Ardhuin & Roland (2012), introducing a simplified accounting of shoreline reflection in a global wave model has identified significant impacts in this region.

- Relatively large errors are present around coastlines, and in semi-enclosed basins. This is partly due to wind errors associated with the transition from land to sea (e.g. Xie et al. 2001; Chelton et al. 2004), but it is also likely due to a known low bias in the Ardhuin et al. (2010) source terms at short fetch (Ardhuin et al. 2010). Deficiencies in the bathymetry may also be a contributing factor.
- The effects of currents on the wave field have been ignored in the model simulations carried out in this work. Over most of the ocean these are negligible; however, more scrutiny is required in areas of strong, persistent currents. On the scales considered here, two current-related effects are of relevance: wave-current interactions and the correct estimation of the true wind speed with respect to the moving sea surface. The relative contribution of the inclusion of each effect was quantified in a recent series of experiments at ECMWF (Hersbach & Bidlot 2008; Bidlot 2010; Bidlot 2012). Though largely speculative, a number of features suggestive of wave-current interactions are evident here. For example, areas of local RMSE maxima can be seen in the regions of the Agulhas return current off the Cape of Good Hope, the Kuroshio current flowing north on the west side of the North Pacific Ocean, the Gulf Stream, flowing north along the west side of the North Atlantic Ocean, and the Antarctic Circumpolar Current (ACC) as it flows through the Drake Passage between the southern tip of South America and the Antarctic Peninsula.

It is also informative to consider the normalized values of these statistics. Figure 11 shows H_s (a) bias and (b) RMSE normalized by the mean H_s . In addition to the observations above, several other notable features are apparent. The first is that while the negative bias in the Western tropical Pacific is quite small in absolute terms (on the order of 10 cm), it is quite large in terms of a percentage of the mean (of the order of 10%), with the feature being more prominent when considered from this perspective. Similarly, while error around coastlines does not stand out in terms of absolute RMSE, when considered in normalised terms, it is clear that coastal error is relatively large.

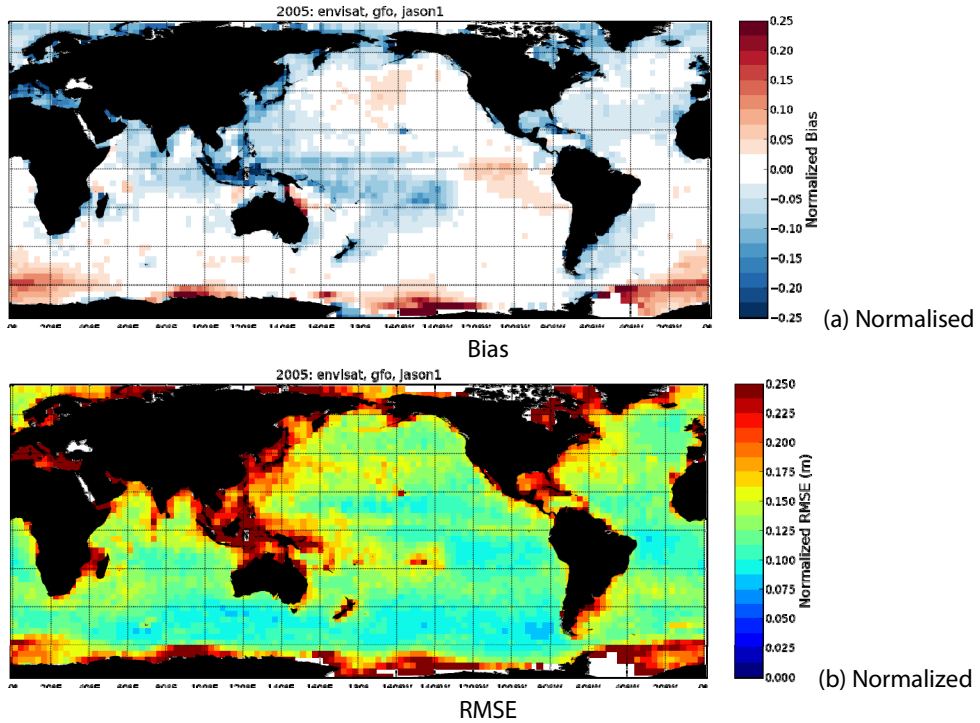


Fig. 11 As Fig. 10, but with H_s (a) bias and (b) RMSE normalized by the mean observed value.

Figure 12 shows the cumulative distribution of grid values from the gridded statistics presented in Fig. 11 (absolute values in the case of the normalized bias). Normalized biases are less than 3% for 50% of the globe, and less than 10% for 90% of the globe. Normalized RMSE is less than 15% for 70% of the grid points, and less than 25% for 90%.

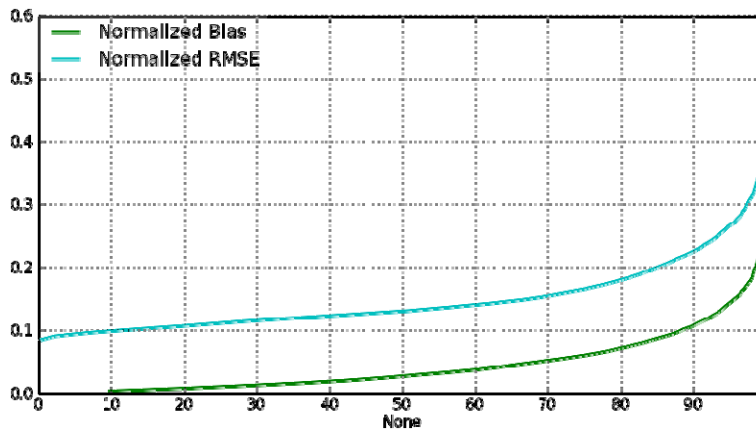


Fig. 12 Cumulative distribution of grid values from 3 x 3° gridded H_s statistics shown in Fig. 11 (a) for normalized bias and (b) normalised RMSE

Considering the variation of error through time, Fig. 13 shows monthly altimeter statistics of H_s for all available altimeter data. In general, agreement between altimeter and the model increases through time, in terms of SI, RMSE and R. This is likely due to two factors: 1) improvements in the winds with time due to increases in the number of observations assimilated and 2) improvements in the observational accuracy with subsequent altimeter missions. Reductions in altimeter scatter are evident, with stepwise reductions from one altimeter to the next, however, examining each altimeter individually, there is also evidence of gradual increases in accuracy through each campaign. This is likely the result of improvement in the CFSR winds through time as the volume and quality of assimilated data increases with improving observations networks.

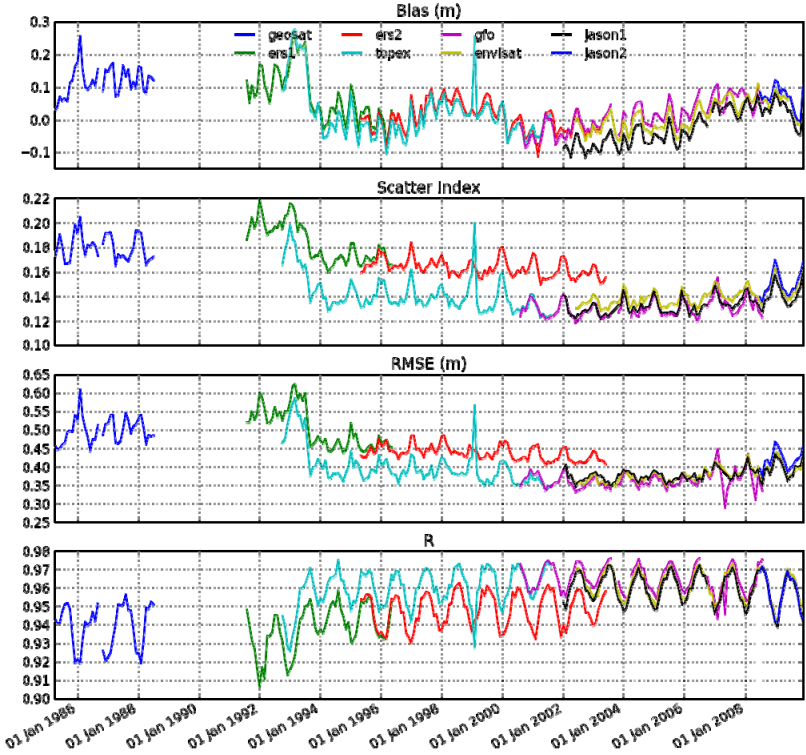


Fig. 13 Monthly model error H_s statistics in reference to altimeter data

In addition to the seasonal patterns, there appears to be notable inter-annual variability. This can most obviously be seen in the bias plot, indicating a positive bias prior to 1993 before an abrupt change to near zero bias, with a gradual increasing bias from 2005 (a year by year plot of spatial bias is given in Appendix C Fig. 20). Given that no alteration is made to the wave model, the obvious suspect for the source of this inconsistency is the forcing winds. Figure 14, showing mean and 80th, 90th, 95th and 99th percentile U_{10} wind speeds for both the Northern and Southern Hemisphere over the full CFSR dataset supports this conclusion. The Northern Hemisphere appears to be reasonably consistent across the record, with some interannual variation, possibly related to large-scale modes of atmospheric variability such as the El-Nino Southern Oscillation (ENSO) and associated

storm activity. In the Southern Ocean, however, superimposed on these fluctuations, a clear stepwise reduction is apparent around 1993/1994. This change is not visible in the mean, but is increasingly apparent in the higher percentile winds. This transition coincides with the introduction of Special Sensor Microwave Imager (SSM/I) derived ocean surface wind observations into the assimilated data stream (Saha et al. 2010), the effect of which is likely felt more strongly in the Southern Hemisphere due to the greater proportion of ocean relative to the Northern Hemisphere.

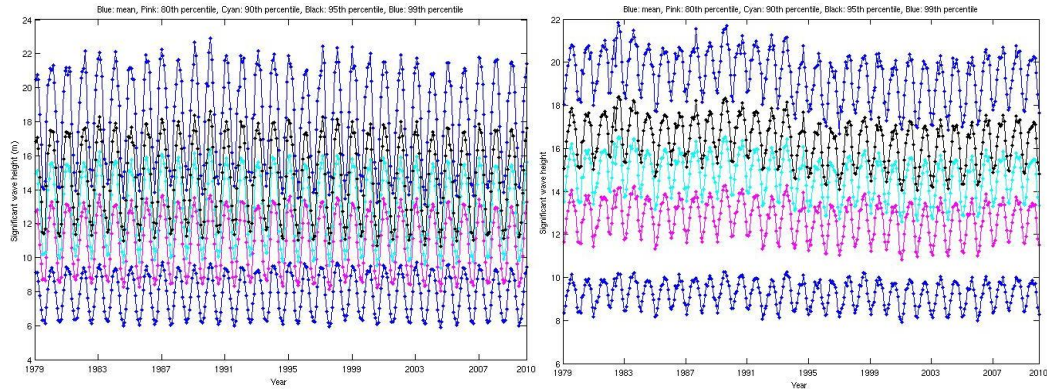


Fig. 14 Monthly mean (blue) and 80th (pink), 90th (cyan), 95th (black) and 99th (blue) percentile U_{10} (m s^{-1})

The fact that these changes are occurring in the upper percentile winds has a disproportionate impact on the resulting modelled waves due to the dominant role that these high winds play in wave generation (e.g. Chawla et al. 2009).

4.2.2 NDBC buoys

As for altimeter observations (above), buoy co-locations are calculated by means of tri-linear interpolation of the hourly model data in space and time to match the observations. Winds are adjusted to 10m heights. Statistics for H_s , U_{10} and T_p for all NDBC buoys for the entire hindcast period are given in Table 3, Table 5, and Table 4 respectively.

H_s bias and RMSE from these buoys are presented spatially in Fig. 15. Overall, results show broad-scale agreement with the altimeter results, with biases being slightly positive on the U.S. west coast, and slightly negative on the east coast and around Hawaii. SI values are typically less than 0.2, and R values around 0.9. QQ-plots, PDFs and scatter density plots for each buoy can be found in Appendix D.

Table 3: H_s statistics for the entire period against selected NDBC buoy observations

Buoy	Obs Mean (m)	Obs Std (m)	Bias (m)	Norm. Bias	SI	RMSE (m)	R	N
<i>U.S. East Coast</i>								
41001	2.04	1.14	-0.07	-0.04	0.18	0.38	0.95	200294
41002	1.84	1.01	-0.04	-0.02	0.19	0.35	0.94	194737
41004	1.32	0.70	0.02	0.01	0.20	0.27	0.93	151136
41008	1.01	0.48	0.06	0.06	0.21	0.22	0.90	150780
41010	1.57	0.83	-0.04	-0.03	0.18	0.28	0.94	231622
42007	0.97	0.45	-0.19	-0.19	0.32	0.36	0.76	59040
44004	2.04	1.25	-0.04	-0.02	0.21	0.42	0.95	196050
44005	1.58	0.98	-0.14	-0.09	0.30	0.50	0.88	219714
44011	2.01	1.21	-0.10	-0.05	0.22	0.46	0.93	197182
44025	1.32	0.73	-0.11	-0.08	0.21	0.30	0.93	157852
<i>Gulf of Mexico</i>								
42001	1.24	0.72	0.03	0.02	0.22	0.28	0.93	214669
42002	1.33	0.71	-0.02	-0.02	0.21	0.28	0.92	221674
42003	1.32	0.70	-0.08	-0.06	0.20	0.27	0.93	170845
<i>U.S. West Coast</i>								
46001	2.74	1.43	0.01	0.00	0.15	0.42	0.96	262099
46002	2.70	1.33	0.10	0.04	0.15	0.41	0.96	220607
46005	2.79	1.45	0.13	0.05	0.15	0.44	0.96	219484
46006	2.83	1.50	0.12	0.04	0.15	0.44	0.96	210995
46011	2.04	0.88	-0.14	-0.07	0.20	0.44	0.88	220545
46012	2.11	0.92	0.34	0.16	0.19	0.52	0.91	219379
<i>Hawaii</i>								
51001	2.41	0.91	-0.07	-0.03	0.17	0.42	0.89	205014
51002	2.40	0.65	-0.04	-0.02	0.15	0.35	0.85	193835
51003	2.21	0.65	-0.10	-0.04	0.17	0.38	0.84	205741
51004	2.40	0.61	-0.12	-0.05	0.12	0.31	0.89	191405

Table 4: U_{10} statistics for the entire period against selected NDBC buoy observations

Buoy	Obs Mean (m s ⁻¹)	Obs Std (m s ⁻¹)	Bias (m s ⁻¹)	Norm. Bias	SI	RMSE (m s ⁻¹)	R	N
<i>U.S. East Coast</i>								
41001	7.90	3.71	0.09	0.01	0.23	1.81	0.88	196495
41002	7.32	3.41	0.16	0.02	0.23	1.72	0.88	211164
41004	7.19	3.40	0.03	0.00	0.24	1.71	0.87	160623
41008	6.17	2.97	0.29	0.05	0.30	1.85	0.80	164718
41010	6.77	3.15	-0.23	-0.03	0.22	1.51	0.88	239654
42007	6.17	2.92	-0.53	-0.09	0.29	1.88	0.79	206565
44004	8.02	3.90	0.28	0.03	0.23	1.85	0.89	191105
44005	7.33	3.80	0.62	0.09	0.26	2.03	0.87	226425
44011	6.88	3.67	0.78	0.11	0.25	1.91	0.89	186671
44025	7.22	3.57	0.04	0.01	0.23	1.66	0.89	183252
<i>Gulf of Mexico</i>								
42001	6.64	3.10	-0.44	-0.07	0.24	1.63	0.86	259477
42002	6.52	2.92	0.03	0.00	0.25	1.62	0.84	252461
42003	6.58	3.14	-0.45	-0.07	0.24	1.62	0.87	245461
<i>U.S. West Coast</i>								
46001	8.14	3.72	0.16	0.02	0.20	1.63	0.91	239448
46002	7.69	3.27	0.06	0.01	0.19	1.44	0.91	221118
46005	8.01	3.57	0.02	0.00	0.19	1.56	0.91	215239
46006	8.26	3.79	-0.21	-0.03	0.19	1.55	0.92	185215
46011	6.34	3.23	-1.42	-0.22	0.34	2.59	0.75	204340
46012	6.11	3.24	1.19	0.19	0.37	2.57	0.78	215772
<i>Hawaii</i>								
51001	7.39	2.63	-0.27	-0.04	0.18	1.35	0.87	202398
51002	8.48	2.39	-0.44	-0.05	0.15	1.31	0.87	205911
51003	6.68	2.22	-0.52	-0.08	0.22	1.53	0.77	206550
51004	8.11	2.20	-0.42	-0.05	0.15	1.32	0.83	191133

Table 5: T_p statistics for the entire period against selected NDBC buoy observations

Buoy	Obs Mean (s)	Obs Std (s)	Bias (s)	Norm. Bias	SI	RMSE (s)	R	N
<i>U.S. East Coast</i>								
41001	8.07	2.05	0.10	0.01	0.22	1.74	0.61	198089
41002	8.09	2.14	0.35	0.04	0.23	1.86	0.59	193765
41004	7.29	2.16	0.65	0.09	0.28	2.14	0.53	150387
41008	7.51	2.68	0.26	0.04	0.31	2.37	0.55	155137
41010	8.15	2.28	0.54	0.07	0.24	2.02	0.56	223293
42007	4.99	1.73	-0.73	-0.15	0.28	1.56	0.62	146052
44004	8.01	2.21	0.02	0.00	0.23	1.83	0.62	194828
44005	7.42	2.37	0.36	0.05	0.32	2.37	0.51	217545
44011	8.20	2.11	-0.15	-0.02	0.22	1.79	0.61	193681
44025	7.25	2.47	0.24	0.03	0.30	2.18	0.58	164170
<i>Gulf of Mexico</i>								
42001	6.08	1.52	0.13	0.02	0.25	1.53	0.47	252574
42002	6.33	1.46	-0.19	-0.03	0.16	1.03	0.73	247172
42003	6.18	1.43	-0.77	-0.12	0.19	1.43	0.60	232735
<i>U.S. West Coast</i>								
46001	9.90	2.66	1.15	0.12	0.33	3.43	0.36	255736
46002	10.92	3.18	1.51	0.14	0.30	3.65	0.43	211322
46005	10.82	3.12	1.35	0.12	0.30	3.49	0.45	212419
46006	11.20	3.11	0.94	0.08	0.26	3.10	0.52	203391
46011	11.45	3.33	1.42	0.12	0.29	3.60	0.47	215381
46012	11.44	3.19	1.10	0.10	0.27	3.25	0.54	216023
<i>Hawaii</i>								
51001	10.56	2.96	1.10	0.10	0.29	3.23	0.50	204960
51002	10.03	2.84	1.52	0.15	0.32	3.57	0.44	192997
51003	10.36	2.93	1.59	0.15	0.30	3.50	0.44	199963
51004	10.15	2.79	1.03	0.10	0.31	3.28	0.47	187698

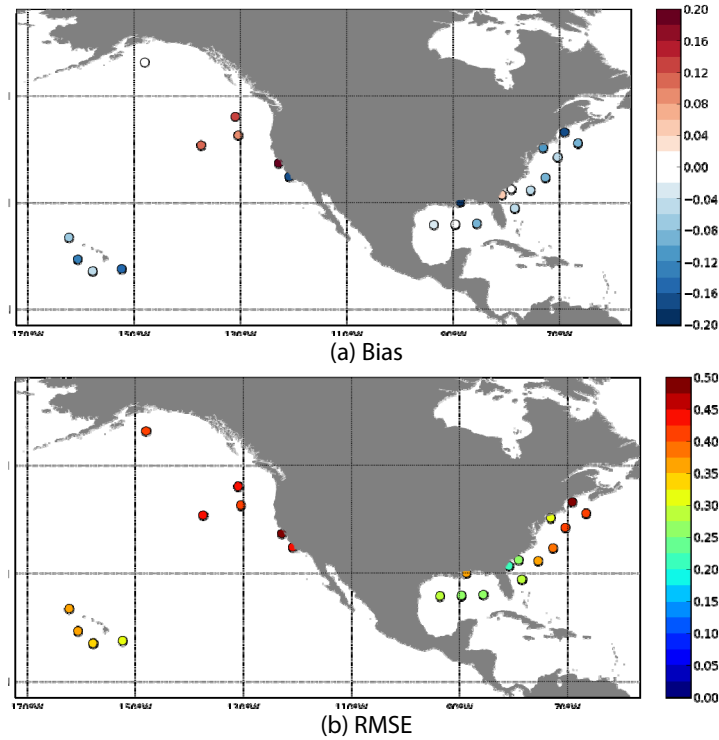


Fig. 15 Model H_s bias (a) and RMSE (b) in meters for the entire hindcast relative to NDBC buoys

U_{10} and T_p also appear to show good agreement with observations. U_{10} results indicate small overall biases, with most buoys showing SI values below 0.3 and RMSE values below 2.0m/s. T_p is a little more varied. However, when considering T_p , it must be noted that this variable is highly discontinuous. For example, in a situation where the spectrum is largely made up of wind-sea, the arrival of swell may cause an abrupt increase of 10 seconds or more in the T_p . Similarly, where the spectrum contains two peaks of similar amplitude, small changes in the underlying energy distribution can result in large changes to the T_p . Thus large differences between the modelled and observed x do not necessarily imply that there are large differences in the spectra. Comparison of individual wave fields (e.g Hanson et al. 2008) would provide more physically meaningful results, however, this is out of scope here.

4.3 South Pacific validations

4.3.1 SOPAC buoys

As described in Section 4.1, several buoy deployments were made in the South Pacific in the late 1980's and the early 1990's. While the short-term nature of these deployments limits the conclusions that can be drawn from these data, they provide a valuable means of validation in the region, adding confidence to the longer term climate work based on this model data undertaken by Trenham et al. (2013). All validations presented here are from data taken from the high resolution 4' grids. These buoys do not measure U_{10} , so only H_s

and T_p are examined here. NDBC buoy 52200, installed near Guam in 2004 also falls inside the 4' grids and is included here. Buoy 151 is too close to land to be resolved by the grid, and is omitted.

Table 6 and Table 7 show validation statistics for H_s and T_p respectively. H_s bias and RMSE are also presented spatially in Fig. 16. Once again, results show broad-scale agreement with the altimeter results. Buoys inside the complex island bathymetry of the South Pacific (16, 32, 33, 37, 52200) show a slight negative bias while those exposed to the Southern Ocean (152, 41) show a slight positive bias. H_s RMSE is less than 50 cm, with SI ranging from 3 to 19%. R values are between 0.8 and 0.9 in most cases. In the case of T_p , as expected in the Tropics, mean T_p is quite high, at between 9 and 12 seconds for the SOPAC buoys, in part accounting for the higher RMSE errors than in the case of the NDBC buoys. A positive bias is evident at all buoys, but it is small. SI is comparable to the NDBC buoys, but R values are significantly lower. The latter may be due to increased incidents of the model and observations identifying different maxima as the peak in the complex spectra containing multiple swell systems expected in the Tropics.

Table 6: Statistics for H_s for the 4' grids against all available SOPAC observations and the Guam NDBC buoy (52200).

Buoy	Obs Mean (m)	Obs Std (m)	Bias (m)	Norm. Bias	SI	RMSE (m)	R	N
37	1.84	0.63	-0.27	-0.15	0.16	0.39	0.89	2966
152	2.26	0.62	0.07	0.03	0.13	0.31	0.88	1052
16	2.16	0.71	-0.07	-0.03	0.19	0.42	0.82	6642
32	1.78	0.54	-0.27	-0.15	0.18	0.42	0.80	6360
33	1.74	0.32	-0.41	-0.24	0.13	0.47	0.69	4558
41	2.13	0.64	0.10	0.05	0.16	0.36	0.85	5563
52200	1.52	0.61	-0.11	-0.08	0.14	0.24	0.95	50160

Table 7: Statistics for T_p for the 4' grids against all available SOPAC observations and the Guam NDBC buoy (52200).

Buoy	Obs Mean (s)	Obs Std (s)	Bias (s)	Norm. Bias	SI	RMSE (s)	R	N
37	9.15	2.27	0.24	0.03	0.26	2.35	0.47	2338
152	11.32	2.64	0.77	0.07	0.24	2.86	0.48	944
16	11.19	2.58	1.89	0.17	0.26	3.50	0.37	1453
32	11.07	2.57	2.54	0.23	0.28	4.04	0.26	4785
33	11.19	2.63	1.26	0.11	0.28	3.34	0.40	4028
41	11.37	2.97	2.00	0.18	0.29	3.89	0.35	4394
52200	8.91	1.87	0.46	0.05	0.19	1.74	0.50	50038

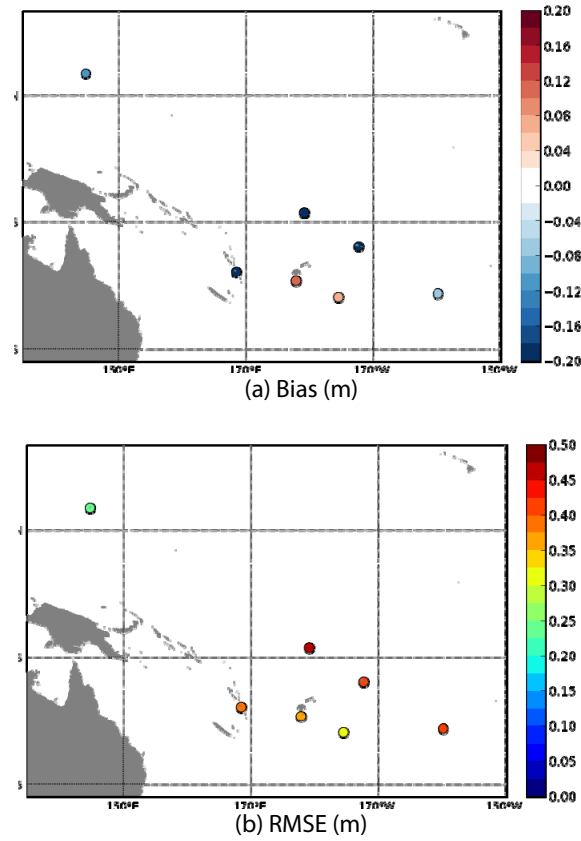


Fig. 16 (a) Bias and (b) RMSE of hindcast H_s from 4' grids against all available SOPAC

There is some variation from buoy to buoy. This can be largely attributed to buoy placement. While all buoys are in deep water (deeper than 100 m), they are often placed very close to land; in some cases, too close to be adequately resolved by the 4' grids used here. Consider for example two cases: buoy 41 off Fiji, where the model is performing well, and 33 off Funafuti in Tuvalu, where the model is performing comparatively poorly. Figure 17 shows the model grids (shown here with the H_s field), as well as a satellite image taken from Google EarthTM. Within the 4' grid, the Fiji buoy is situated several grid points offshore in a position that is well resolved by the grid. The Funafuti atoll by contrast is not well resolved. The Tuvalu buoy is located just to the east of the largest atoll, Funafuti, consisting of a narrow sweep of land between 20 and 400 metres wide, encircling a large lagoon 18 km long and 14 km wide. The land area of the 33 islets aggregates to 2.4 km², less than one per cent of the total area of the atoll. This presents a challenging situation to explicitly resolve, with individual surface penetrating parts of the reef being very small in scale, yet collectively amounting to a significant obstacle for propagating waves. Imperfect bathymetry is also likely to be a significant source of error. While the effect of this total wave energy blocking is apparently accounted for by the sub-grid-scale parameterisation, we might expect that the model would not capture the wave field at the buoy location well. This is confirmed by Fig.18 showing QQ-plots, PDFs, scatter density plots and time series constructed from the full buoy record for each buoy (similar plots for all SOPAC buoys are given in Appendix E). In the case of the Fiji buoy, agreement between model and

observations is high; QQ, PDF and scatter density plots indicate good agreement throughout the range of wave heights. At Tuvalu on the other hand the model clearly shows a negative bias, as well as an inability to capture the variability in the time series.

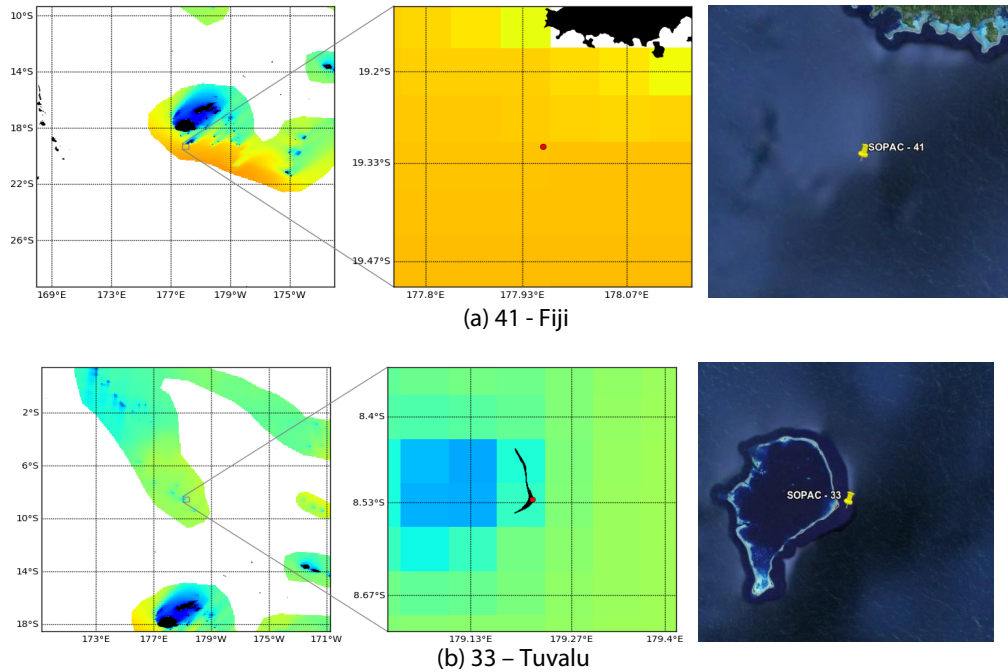


Fig. 17 Model grids and Google Earth™ images of SOPAC buoys (a) 41 - Fiji and (b) 33 – Tuvalu. Grids are shown with an example H_s field plotted. Black land is added by the plotting software for reference only, the model land-mask can be seen by white areas of missing data.

Overall the validations against SOPAC buoys indicate a high degree of model skill for the grids with 4' resolution. While some of the finer details of the wave field cannot be resolved at this resolution, it has been shown that at a reasonable distance offshore, the hindcast data is highly accurate. This provides confidence in the provision of spectral data as boundary conditions for finer scale models which could better resolve the coastal variability where required.

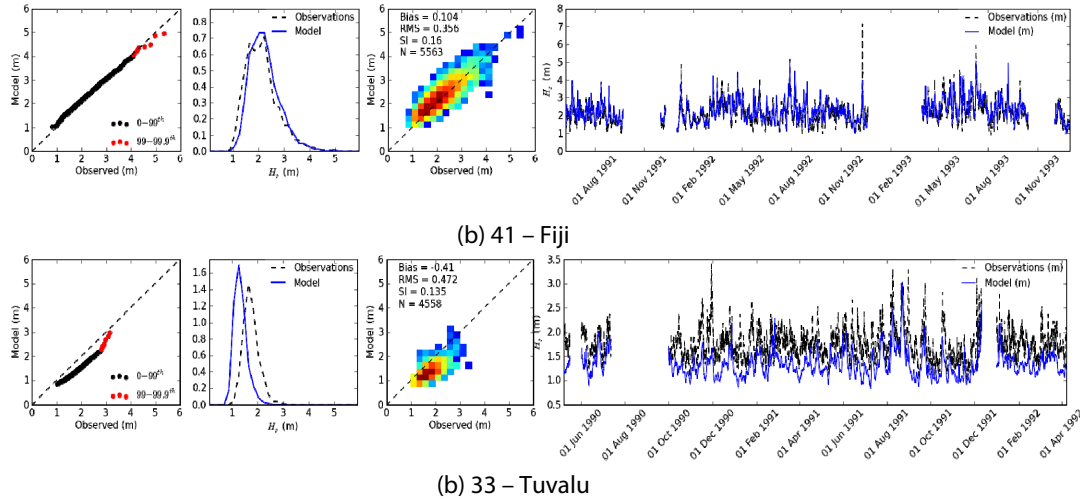


Fig. 18 H_s qq-plot, pdf, scatter density plot and time series plot of SOPAC buoys (a) 41 off Fiji and (b) 33 off Tuvalu.

5. CONCLUSIONS AND OUTLOOK

This report outlines the 31 year wave hindcast has been produced using the WAVEWATCH III model forced by CFSR reanalysis winds. The resulting archive consists of a comprehensive database of integrated variables, with the number of fields available far exceeding previous hindcasts. Data is archived hourly, at 0.4° over the globe and high resolution outputs down to $4'$ over the South Pacific and around the Australian coast, again, far higher temporal and spatial resolution than has previously been achieved. Additionally, a large number of spectral output points have also been archived, concentrated in the South Pacific and Australian regions.

Validation has been carried out against all available altimeter data, a selection of NDBC buoys, and a number of short-term buoy deployments in the South Pacific. Concentrating mainly on H_s , the hindcast data show generally excellent agreement, up to the 99.9th percentile. Some concern arises with a discontinuity clearly present in the CFSR winds. This mainly affects the high wind speeds, with an apparent step change around 1993, and a slowly increasing positive trend after 2000. This results in an over-prediction of wave heights in the mid-latitudes in the early part of this hindcast, and a slight over-prediction in the last few years.

Validation presented here is by no means exhaustive. In future work, further validation of the high-resolution data around the Australian coast will be carried out against buoys from the Australian network. Further validation of wave spectral data would also be of great benefit. This work has concentrated on overall statistics; more work is required to examine the performance of this hindcast in terms of specific events such as strong mid-latitude storms and tropical cyclones. The hindcast will also be extended to mid-2013 in the near future.

It is hoped that this data will provide the basis for many further wave studies in the Pacific. The data presented here provides the first long term wave hindcast of sufficient resolution

to capture the wave field accurately within the complex island chains of the Central and South Pacific. It provides the ideal data from which to construct wind-wave climatologies for the region. Indeed, such work has been conducted for a small number of locations as part of the PACCSAP work in the Updated Country Reports (Trenham et. al, 2013). This database provides perhaps the first with which the damaging swells in the region can be reliably examined. Hoeke et al. (2013) for example, have identified five inundation events, which were a consequence of extra-tropical storm generated waves propagating into the region, resulting in coastal flooding. These events span three areas of interest in the Pacific, impacting on at least five Pacific Island Countries. Reported swell-driven flooding events in the Indian (Maldives) and Atlantic (Ascension) Oceans also provide examples of damaging swell events. This wave hindcast provides a unique dataset with which to study these events and develop a greater understanding of wave impacts in the region. The output of spectral partitions allows for the identification of the source location of swells associated with the identified surge events (following Delpy, Ardhuin, Collard, & Chapron, (2010) for example), thereby allowing the climatological drivers of such events to be identified, and seasonal prediction system to be developed.

The large number of spectral outputs provides up-to-date boundary conditions that can be used to drive coastal models in the region to investigate storm surge and flood risks. In the future, wave modelling could be combined with other physical processes such as sea-level change and inundation studies, as well as biogeochemistry and ecology, to understand environmental stressors in the region, and potentially to make integrated climate projections for individual islands.

REFERENCES

- Ardhuin, F., Chapron, B., & Collard, F. 2009. Observation of swell dissipation across oceans. *Geophysical Research Letters*, 36(6), 1–6. doi:10.1029/2008GL037030
- Ardhuin, F., Rogers, W. E., Babanin, A. V, Filipot, J.-F., Magne, R., Roland, A., van der Westhuysen, A, Queffeuilou, P, Lee, B, Aouf, L, Collard, F. 2010. Semiempirical Dissipation Source Functions for Ocean Waves. Part I: Definition, Calibration, and Validation. *Journal of Physical Oceanography*, 40(9), 1917–1941. doi:10.1175/2010JPO4324.1
- Ardhuin, F., Tournadre, J., Queffeuilou, P., Girard-Ardhuin, F., & Collard, F. 2011. Observation and parameterization of small icebergs: drifting breakwaters in the Southern Ocean. *Ocean Modelling*, 1, 2–7. doi:10.1016/j.ocemod.2011.03.004
- Ardhuin, F., & Roland, A. 2012. Coastal wave reflection, directional spread, and seismoacoustic noise sources. *Journal of Geophysical Research*, 117, 1–16. doi:10.1029/2011JC007832
- Banner, M. L., & Morison, R. P. 2010. Refined source terms in wind wave models with explicit wave breaking prediction. Part I: Model framework and validation against field data. *Ocean Modelling*, 33(1-2), 177–189. doi:10.1016/j.ocemod.2010.01.002
- Barstow, S.F. and Haug, O. 1994a. The Wave Climate of Fiji. *SOPAC Tech. report*, 205.
- Barstow, S.F. and Haug, O. 1994b. The Wave Climate of the Cook Islands. *SOPAC Tech. report*, 200.
- Barstow, S.F. and Haug, O. 1994c. The Wave Climate of the Kingdom of Tonga. *SOPAC Tech. report*, 201.
- Battjes, J.A. and Janssen, P.A.E.M. 1978. Energy loss and set-up due to breaking of random waves. In *cedb.asce.org*. pp. 569–587.
- Bender, L.C. 1996. Modification of the physics and numerics in a third-generation ocean wave model. *Journal of Atmospheric and Oceanic Technology*, 13, pp.726–750.
- Bidlot, J.-R., Holmes, D. J., Wittmann, P. A., Lalbeharry, R., Chen, H. S. 2002. Intercomparison of the performance of operational ocean wave forecasting systems with buoy data. *Weather and Forecasting*, 17, 287–310.
- Bidlot, J.-R., Li, J. G., Wittmann, P., Fauchon, M., Chen, H. S., Lefevre, J.-M., Greenslade, D J M, Bruns, T., Ardhuin, F Kohno, N, Sanwook, P, Marta, G, 2007. Inter-comparison of operational wave forecasting systems. *Proceedings, 10th Int. Workshop of Wave Hindcasting and Forecasting, Hawaii*, 1–22.
- Bidlot, J.-R. 2010. Use of MERCATOR surface currents in the ECMWF forecasting system. *ECMWF Research Department Memorandum*, R60.9/JB/1.

- Bidlot, J.-R. 2012. Use of MERCATOR surface currents in the ECMWF forecasting system: a follow-up study. *ECMWF Research Department Memorandum*, R60.9/JB/1.
- Bidlot, J.-R., Janssen, P. and Abdalla, S. 2005. A revised formulation for ocean wave dissipation in CY29R1. *ECMWF Technical Memorandum*, R60.9/JB/0(1), pp.1–35.
- Caires, S. and Sterl, A. 2005. A New Nonparametric Method to Correct Model Data: Application to Significant Wave Height from the ERA-40 Re-Analysis. *Journal of Atmospheric and Oceanic Technology*, 22(4), 443–459. doi:10.1175/JTECH1707.1
- Caires, S., and Sterl, A., 2003. Validation of ocean wind and wave data using triple collocation. *Journal of Geophysical Research*, 108(C3), 3098. doi:10.1029/2002JC001491
- Cardone, V. J., Jensen, R. E., Resio, D. T., Swail, V. R., and Cox, A. T. (1996). Evaluation of contemporary ocean wave models in rare extreme events: The Halloween storm' of October 1991 and the storm of the century' of March 1993. *Journal of Atmospheric and Oceanic Technology*, 13, 198–230.
- Cavaleri, L. 2009. Wave Modeling - Missing the Peaks. *Journal of Physical Oceanography*, 39(11), 2757. doi:10.1175/2009JPO4067.1
- Chalikov, D.V. 1995. The parameterization of the wave boundary layer. *Journal of Physical Oceanography*, 25(6), pp.1333–1349.
- Chalikov, D.V and Belevich, M.Y. 1993. One-dimensional theory of the wave boundary layer. *Boundary-Layer Meteorology*, 63(1), pp.65–96.
- Chawla, A. et al. 2009. Validation of a Multi-Grid WAVEWATCH III Modeling System. In *11th International Workshop on Wave Hindcasting and Forecasting & Coastal Hazards Symposium, Halifax, Canada October 18-23*.
- Chawla, A., Tolman, H. L., Hanson, J. L., Devaliere, E., and Gerald, V. M. 2009. Validation of a Multi-Grid WAVEWATCH III Modeling System. In *Proceedings of the 11th International Workshop on Wave Hindcasting and Forecasting & Coastal Hazards Symposium, Halifax, Canada October 18-23*.
- Chawla, A., Spindler, D.M. and Tolman, H.L. 2012. Validation of a thirty year wave hindcast using the Climate Forecast System Reanalysis winds. *Ocean Modelling*. doi:10.1016/j.ocemod.2012.07.005
- Chawla, A., & Tolman, H. L., 2008. Obstruction Grids for Spectral Wave Models. *Ocean Modelling*, 22, 12–25. doi:10.1016/j.ocemod.2008.01.003
- Chelton, D. B., Schlax, M. G., Freilich, M. H., & Milliff, R. F., 2004. Satellite measurements reveal persistent small-scale features in ocean winds. *Science*, 303(5660), 978–83. doi:10.1126/science.1091901

- Chelton, D.B. and Freilich, M.H. 2005. Scatterometer-based assessment of 10-m wind analyses from the Operational ECMWF and NCEP Numerical Weather Prediction Models. *Monthly Weather Review*, 133, pp.409–429.
- Chen, G., Chapron, B., Ezraty, R., & Vandemark, D., 2002. A global view of swell and wind sea climate in the ocean by satellite altimeter and scatterometer. *Journal of Atmospheric and Oceanic Technology*, 19, 1849–1859.
- Chen, G. and Belcher, S.E. 2000. Effects of long waves on wind-generated waves. *Journal of physical oceanography* (1974), pp.2246–2256.
- Collard, F., Ardhuin, F., & Chapron, B., 2009. Monitoring and analysis of ocean swell fields from space: New methods for routine observations. *Journal of Geophysical Research*, 114(C7), 1–15. doi:10.1029/2008JC005215
- Cotton, P.D. and Carter, D.J.T. 1994. Cross calibration of TOPEX, ERS-1, and GEOSAT wave heights. *Journal of Geophysical Research*, 99, pp.25025–25033.
- Cox, A.T., Cardone, V.J. and Swail, V.R. 2011. On the use of the climate forecast system reanalysis wind forcing in ocean response modeling. In *12th International Workshop on Wave Hindcasting and Forecasting & 3rd Coastal Hazards Symposium*. p. pp. 20, Paper G3.
- Dee, D. P., Uppala, S. M., Simmons, a. J., Berrisford, P., Poli, P., Kobayashi, S., Andrae, U., Balmaseda, M. a., Balsamo, G., Bauer, P., Bechtold, P., Beljaars, a. C. M., van de Berg, L., Bidlot, J., Bormann, N., Delsol, C., Dragani, R., Fuentes, M., Geer, a. J., Haimberger, L., Healy, S. B., Hersbach, H., Hólm, E. V., Isaksen, L., Kållberg, P., Köhler, M., Matricardi, M., McNally, a. P., Monge-Sanz, B. M., Morcrette, J.-J., Park, B.-K., Peubey, C., de Rosnay, P., Tavolato, C., Thépaut, J.-N., Vitart, F., 2011. The ERA-Interim reanalysis: configuration and performance of the data assimilation system. *Quarterly Journal of the Royal Meteorological Society*, 137(656), 553–597. doi:10.1002/qj.828
- Delpey, M.T., Ardhuin, F., Collard, F. and Chapron, B. 2010. Space-time structure of long ocean swell fields. *Journal of Geophysical Research*, 115(C12), 1–13. doi:10.1029/2009JC005885
- Durrant, T.H., Greenslade, D.J.M. and Simmonds, I. 2013. The effect of statistical wind corrections on global wave forecasts. *Ocean Modelling*, 70, 116–131. doi:10.1016/j.ocemod.2012.10.006
- Durrant, T.H. and Greenslade, D.J.M. 2012. Spatial Evaluations of ACCESS Marine Surface Winds using Scatterometer Data. *Aust. Met, and Ocean. Journal*, (62), pp.263–276.
- Durrant, T. H., Greenslade, D. J. M., & Simmonds, I. 2009. Validation of Jason-1 and Envisat Remotely Sensed Wave Heights. *Journal of Atmospheric and Oceanic Technology*, 26(1), 123. doi:10.1175/2008JTECHO598.1

Elgar, S., Herbers, T.H.C. and Guza, R. T. 1994. Reflection of Ocean Surface Gravity Waves from a Natural Beach. *Journal of Physical Oceanography*, 24(7), 1503–1511. doi:10.1175/1520-0485(1994)024<1503:ROOSGW>2.0.CO;2

Hanson, J. L., Tracy, B. A., Tolman, H. L., & Scott, R. D. 2008. Pacific Hindcast Performance of Three Numerical Wave Models. *Journal of Atmospheric and Oceanic Technology*, 26(8), 1614. doi:10.1175/2009JTECHO650.1

K. Hasselmann, T. P. Barnett, E. Bouws, H. Carlson, D. E. Cartwright, K. Enke, J. A. Ewing, H. Gienapp, D. E. Hasselmann, P. Kruseman, A. Meerburg, P. Müller, D. J. Olbers, K. Richter, W. Sell, and H. Walden, 1973). Measurements of wind-wave growth and swell decay during the Joint North Sea Wave Project (JONSWAP). *Ergänzungsheft Zur Deutschen Hydrographischen Zeitschrift Reihe*, 8(12).

Hasselmann, S., Hasselmann, K., Allender, J., & Barnett, T., 1985. Computation and parameterizations of the nonlinear energy transfer in a gravity-wave spectrum. Part II: Parameterizations of the nonlinear energy transfer for application in wave models. *Journal of Physical Oceanography*, 15, 1378–1391.

Hemer, M., Katzfey, J. and Hotan, C. 2011. *The wind-wave climate of the Pacific Ocean, PASAP final report*. Canberra: DCCEE.

Hemer, M., Church, J., & Hunter, J. 2010. Variability and trends in the directional wave climate of the Southern Hemisphere. *International Journal of Climatology* 491 doi:10.1002/joc.1900

Hersbach, H. and Bidlot, J.-R. 2008. The relevance of ocean surface current in the ECMWF analysis and forecast system. In *Workshop on Ocean-Atmosphere Interactions*. pp. 61–73.

Hoeke, R.K., McInnes, K.L., Kruger, J.C., McNaught, R.J., Hunter, J.R. and Smithers, S.G. 2013. Widespread inundation of Pacific islands triggered by distant-source wind-waves. *Global and Planetary Change*, 108, 128–138. doi:10.1016/j.gloplacha.2013.06.006

Janssen, P.A.E.M. et al. 1994. Parameterization of source terms and the energy balance in a growing wind sea. In *Dynamics and Modelling of Ocean Waves*. Cambridge University Press.

Janssen, P.A.E.M. 1991. Quasi-linear Theory of Wind-Wave Generation Applied to Wave Forecasting. *Journal of Physical Oceanography*, 21, pp.1631–1642.

E. Kalnay, M. Kanamitsu, R. Kistler, W. Collins, D. Deaven, L. Gandin, M. Iredell, S. Saha, G. White, J. Woollen, Y. Zhu, A. Leetmaa, R. Reynolds, M. Chelliah, W. Ebisuzaki, W. Higgins, J. Janowiak, K. C. Mo, C. Ropelewski, J. Wang, R. Jenne, and D. Joseph, 1996: The NCEP/NCAR 40-Year Reanalysis Project.. *Bulletin of the American Meteorological Society*, 77, 437–471.
doi: [http://dx.doi.org/10.1175/1520-0477\(1996\)077<0437:TNYRP>2.0.CO;2](http://dx.doi.org/10.1175/1520-0477(1996)077<0437:TNYRP>2.0.CO;2)

Kanamitsu, M., Ebisuzaki, W., Woollen, J., Yang, S.-K., Hnilo, J. J., Fiorino, M., & Potter, G. L. (2002). NCEP–DOE AMIP-II Reanalysis (R-2). *Bulletin of the American Meteorological Society*, 83(11), 1631–1643. doi:10.1175/BAMS-83-11-1631

Komen, G., Hasselmann, S. and Hasselmann, K. 1984. On the existence of a fully developed wind-sea spectrum. *Journal of Physical. Oceanography*, 14(8), pp.1271–1285.

Leonard, B. 1979. A stable and accurate convective modelling procedure based on quadratic upstream interpolation. *Computer methods in applied mechanics and engineering*, 19(1), pp.59–98.

Leonard, B. 1991. The ULTIMATE conservative difference scheme applied to unsteady one-dimensional advection. *Computer methods in applied mechanics and engineering*, 88(1), pp.17–74.

NRL, 2006. Digital bathymetry data base 2-minute resolution v. 3 (DBB2). Available at: http://www7320.nrlssc.navy.mil/DBDB2_WWW/NRLCOM_dbdb2.html [Accessed April 30, 2009].

Queffeuilou, P. and Croizé-fillon, D. 2012. Global Altimeter SWH data set - Version 9.0. *IFREMER Tech Report*, (April), pp.1–8.

Rasclé, N. and Ardhuin, F. (2013). A global wave parameter database for geophysical applications. Part 2: Model validation with improved source term parameterization. *Ocean Modelling*, 70, 174–188. doi:10.1016/j.ocemod.2012.12.001

Rogers, W.E. and Wittmann, P. 2002. Quantifying the Role of Wind Field Accuracy in the US Navy's Global Ocean Wave Nowcast/Forecast System. *Naval Research Lab Tech Report*, (NRL/MR/732-02-8290).

Saha, S. Moorthi, H.-L. Pan, X. Wu, J. Wang, S. Nadiga, P. Tripp, R. Kistler, J. Woollen, D. Behringer, H. Liu, D. Stokes, R. Grumbine, G. Gayno, J. Wang, Y.-T. Hou, H.-Y. Chuang, H.-M. H. Juang, J. Sela, M. Iredell, R. Treadon, D. Kleist, P. Van Delst, D. Keyser, J. Derber, M. Ek, J. Meng, H. Wei, R. Yang, S. Lord, H. Van Den Dool, A. Kumar, W. Wang, C. Long, M. Chelliah, Y. Xue, B. Huang, J.-K. Schemm, W. Ebisuzaki, R. Lin, P. Xie, M. Chen, S. Zhou, W. Higgins, C.-Z. Zou, Q. Liu, Y. Chen, Y. Han, L. Cucurull, R. W. Reynolds, G. Rutledge, and M. Goldberg., 2010. The NCEP climate forecast system reanalysis. *Bulletin of the American Meteorological Society*, 91(8), 1015–1057.

Tolman, H.L. 1991. A Third-Generation Model for Wind Waves on Slowly Varying, Unsteady, and Inhomogeneous Depths and Currents. *Journal of Physical Oceanography*, 21(6), pp.782–797.

Tolman, H.L. and Chalikov, D.V. 1996. Source Terms in a Third-Generation Wind Wave Model. *Journal of Physical Oceanography*, 26, pp.2497–2518.

Tolman, H.L. 2002a. Alleviating the Garden Sprinkler Effect in wind wave models. *Ocean Modelling*, 4, pp.269–289.

Tolman, H.L. 2002b. Validation of WAVEWATCH III version 1.15 for a global domain. *Tech. Note 213, NOAA/NWS/NCEP/MMAB*.

Tolman, H. L., 2003. Treatment of unresolved islands and ice in wind wave models. *Ocean Modelling*, 5(3), 219–231. doi:10.1016/S1463-5003(02)00040-9

Tolman, H. L. 2008. A mosaic approach to wind wave modeling. *Ocean Modelling*, 25(1-2), 35–47. doi:10.1016/j.ocemod.2008.06.005

Tolman, H.L. 2009. User manual and system documentation of WAVEWATCH III TM version 3.14. *Tech. Note 276, NOAA/NWS/NCEP/MMAB*.

Trenham, C.E., Hemer, M.A., Durrant, T.H. and Greenslade, D.J.M. 2013. PACCSAP Wind-wave Climate: High resolution wind-wave climate and projections of change in the Pacific region for coastal hazard assessments, *CAWCR Technical Report no. 067*.

Uppala, S. M., P. W. K  llberg, a. J. Simmons, U. Andrae, V. D. C. Bechtold, M. Fiorino, J. K. Gibson, J. Haseler, a. Hernandez, G. a. Kelly, X. Li, K. Onogi, S. Saarinen, N. Sokka, R. P. Allan, E. Andersson, K. Arpe, M. a. Balmaseda, a. C. M. Beljaars, L. Van De Berg, J. Bidlot, N. Bormann, S. Caires, F. Chevallier, a. Dethof, M. Dragosavac, M. Fisher, M. Fuentes, S. Hagemann, E. H  lm, B. J. Hoskins, L. Isaksen, P. a. E. M. Janssen, R. Jenne, a. P. McNally, J.-F. Mahfouf, J.-J. Morcrette, N. a. Rayner, R. W. Saunders, P. Simon, a. Sterl, K. E. Trenberth, a. Untch, D. Vasiljevic, P. Viterbo, and J. Woollen, 2005. The ERA-40 re-analysis. *Quarterly Journal of the Royal Meteorological Society*, 131(612), 2961–3012. doi:10.1256/qj.04.176

Xie, S. P., Liu, W. T., Liu, Q., & Nonaka, M., 2001. Far-reaching effects of the Hawaiian Islands on the Pacific Ocean-atmosphere system. *Science*, 292(5524), 2057–60. doi:10.1126/science.1059781

Young, I.R. 1999. Seasonal variability of the global ocean wind and wave climate. *International Journal of Climatology*, 19, pp.931–950.

Young, I.R. and Babanin, A.V. 2006. Spectral distribution of energy dissipation of wind-generated waves due to dominant wave breaking. *Journal of physical oceanography*, 36, pp.376–394.

Young, I. R., Zieger, S., & Babanin, a V., 2011. Global trends in wind speed and wave height. *Science (New York, N.Y.)*, 332(6028), 451–5. doi:10.1126/science.1197219

APPENDIX A MODEL TUNING

The WAM4 input term of Janssen (2004) is as follows:

$$S_{in}(k, \theta) = \frac{\rho_a \beta_{max}}{\rho_w \kappa^2} e^Z Z^4 \left(\frac{u_*}{c} + z_\alpha\right)^2 \cos^{p_{in}}(\theta - \theta_u) \sigma N(k, \theta) + S_{out}(k, \theta) \quad (7)$$

where u_* is the friction velocity ρ_a and ρ_w are the air and water densities, β_{max} is a non-dimensional growth parameter (constant), κ is von Karman's constant, and p_{in} is a constant that controls the directional distribution of S_{in} and Z relates wind speed to u_* . A more complete description of this term can be found in Janssen (1991) and Tolman (2009). The Ardhuin et al. (2010) parameterization uses a positive part of this term, with an ad hoc reduction of u_* implemented in order to allow a balance with a saturation-based dissipation. This correction also reduces the drag coefficient at high winds. This is done by reducing the wind input for high frequencies and high winds. For this, u_* in Equation 5 is replaced by $u'_*(k)$ defined for each frequency as:

$$(u'_*)^2 = \left| u_*^2 (\cos \theta_u, \sin \theta_u) - |s_u| \int_0^k \int_0^{2\pi} \frac{S_{in}(k', \theta)}{c} (\cos \theta, \sin \theta) d\theta dk' \right| \quad (8)$$

Some recommended tunings for CFSR winds are present in the WAVEWATCH III manual (TEST451f), and these tunings are largely adopted here. However, before conducting the full 30 year hindcast, a number of tunings were tested for the full calendar year of 2008.

Figures 19, 20 and 21 show the global spatial bias and QQ-plot calculated from all co-locations for the year of 2008 relative to altimeter data. The first (Fig. 19) shows results using the default tunings. This clearly shows a positive bias, most notably in the storm belts of the mid-latitudes, particularly in the Southern Ocean.

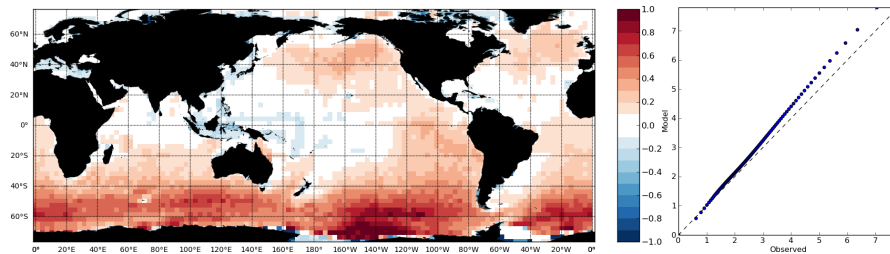


Fig. 19 Global bias (m) on the left and global qq-plot on the right for modelled H_s compared to altimeter for the year of 2008 using default tunings for the Ardhuin 2010 source terms.

First order tuning of the input term is done using the β_{max} term, providing a bulk adjustment to the strength of the input term (e.g. Ardhuin et. al. 2010). Following the recommended tuning for CFSR winds, reducing β_{max} from 1.52 to 1.33 produces significant improvement, as shown in Fig. 20. However, while the positive bias in the northern mid-latitudes has been almost eliminated, a strong positive bias in the Southern Ocean remains. From the QQ-plots, it appears that this bias is present mainly in the upper quartiles of the wave range.

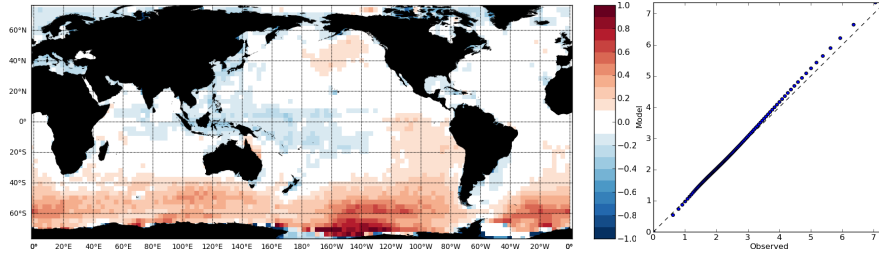


Fig. 20 Same as Fig. 19 but with reduced β_{max} from from 1.52 to 1.33

This was addressed by adjusting in the s_u parameter from Equation 8 controlling the strength of the sheltering effect at high wind speeds. Figure 21 indicates further improvement from this change.

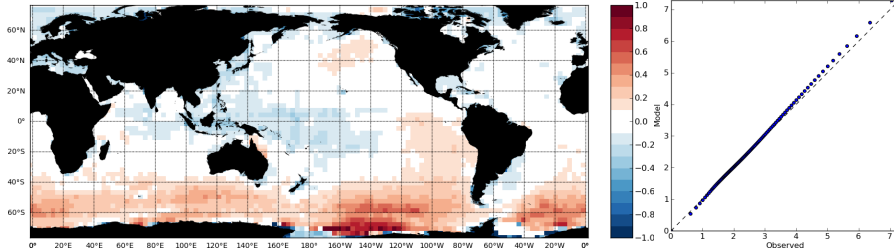


Fig. 21 Same as Fig. 20 but for model run with increased sheltering coefficient s_u from 1.0 to 1.2

While further improvement could arguably be gained from further increasing the sheltering coefficient s_u , this tuning was settled on for several reasons. The first was that some over-estimation of waves in the Southern Ocean is expected due to a lack of direct accounting of wave blocking due to the presence of icebergs (though this is expected to be restricted closer to the ice edge, as discussed in Section 4.2.1). The second is that we know that the CFSR wind biases vary throughout the 30 year period examined here, especially at high wind speeds (discussed in Section 4.2.1), with 2008 sitting in a period of marginally increased positive bias. The third is that decreasing the positive bias in the mid-latitudes tended to increase the negative bias in the Central Pacific. Though this negative bias can likely be explained by a lack of shoreline reflection in the model, given that this was our primary area of interest, we are reluctant to further enhance the problem. Overall, this tuning was deemed optimal.

APPENDIX B ACCESS DETAILS

The wave hindcast is available through <https://data.csiro.au/dap/>, with DOI: <http://dx.doi.org/10.4225/08/523168703DCC5>

Gridded data are separated into monthly files for each grid with the following naming convention:

ww3.<grid_name>.<yyymm>.nc

The names of the grids are as follows:

glob_24m – 24' (0.4°) global grid

aus_10m – 10' around the Australian coastline

aus_4m – 4' around the Australian coastline

pac_10m – 10' in the Pacific

pac_4m – 4' in the Pacific

Files can be downloaded as full files in compressed NetCDF4 format using HDF5 compression. Alternatively, files are hosted on an OPeNDAP server, and individual fields, regions and times can be extracted using standard OPeNDAP calls. The full list of available variables is given in Table 8.

All spectral points are saved in a single file per month:

ww3.<yyymm>_spec.nc

For each output point, the data consists of an hourly time series of the two dimensional spectra, (E_{fth}: sea surface wave directional variance spectral density). Output is at the native spectral resolution that the model is run, i.e. 29 frequencies exponentially spaced from 0.038 Hz to 0.5 Hz and 24 directions with a constant 15° directional resolution. In addition to E_{fth}, each point also has a time series of depth, D_p, U₁₀, wind direction, as well as current speed and direction (both of which are zero here).

Table 8: List of gridded variables available from hindcast

Variable Name	netCDF name	unit
Eastward wind	U10	m/s
Northward wind	V10	m/s
Sea ice fraction	CI	-
Significant wave height	hs	m
Mean wave length	wl	m
Mean period	T	s
Wave energy flux	CgE	kW/m
Wave peak frequency	fp	Hz
Wave mean direction	dir	degree
Directional spread	spr	degree
Peak direction	dp	degree
Significant wave height of wind sea	hs0	m
Significant wave height of primary, secondary and tertiary swell	hs1-3	m
Peak period of wind sea	tp0	s
Peak period of primary, secondary and tertiary swell	tp1-3	s
Mean wave length of wind sea	lp0	m
Mean wave length of primary, secondary and tertiary swell	lp1-3	m
Wave mean direction of wind sea	th0	degree
Wave mean direction of primary, secondary and tertiary swell	th1-3	degree
Directional spread of wind sea	si0	degree
Directional spread of primary, secondary and tertiary swell	si1-3	degree
Wind sea fraction of wind sea	ws0	-
Wind sea fraction of primary, secondary and tertiary swell	ws1-3	-
Wind sea fraction	ws	-
Number of wave partitions	npr	-
Eastward friction velocity	uust	m/s
Northward friction velocity	vust	m/s
Charnock coefficient	cha	-
Wind to wave energy flux	faw	Wm ⁻²
Eastward surface stokes drift	uuss	m/s
Northward surface stokes drift	vuss	m/s

APPENDIX C ADDITIONAL ALTIMETER VALIDATION RESULTS

Plots in this appendix include spatial model H_s bias (Fig. 22) and QQ-plots, PDF's and scatter density plots (Fig. 23) calculated from model-altimeter co-locations separately for each year covered by the altimeter record.

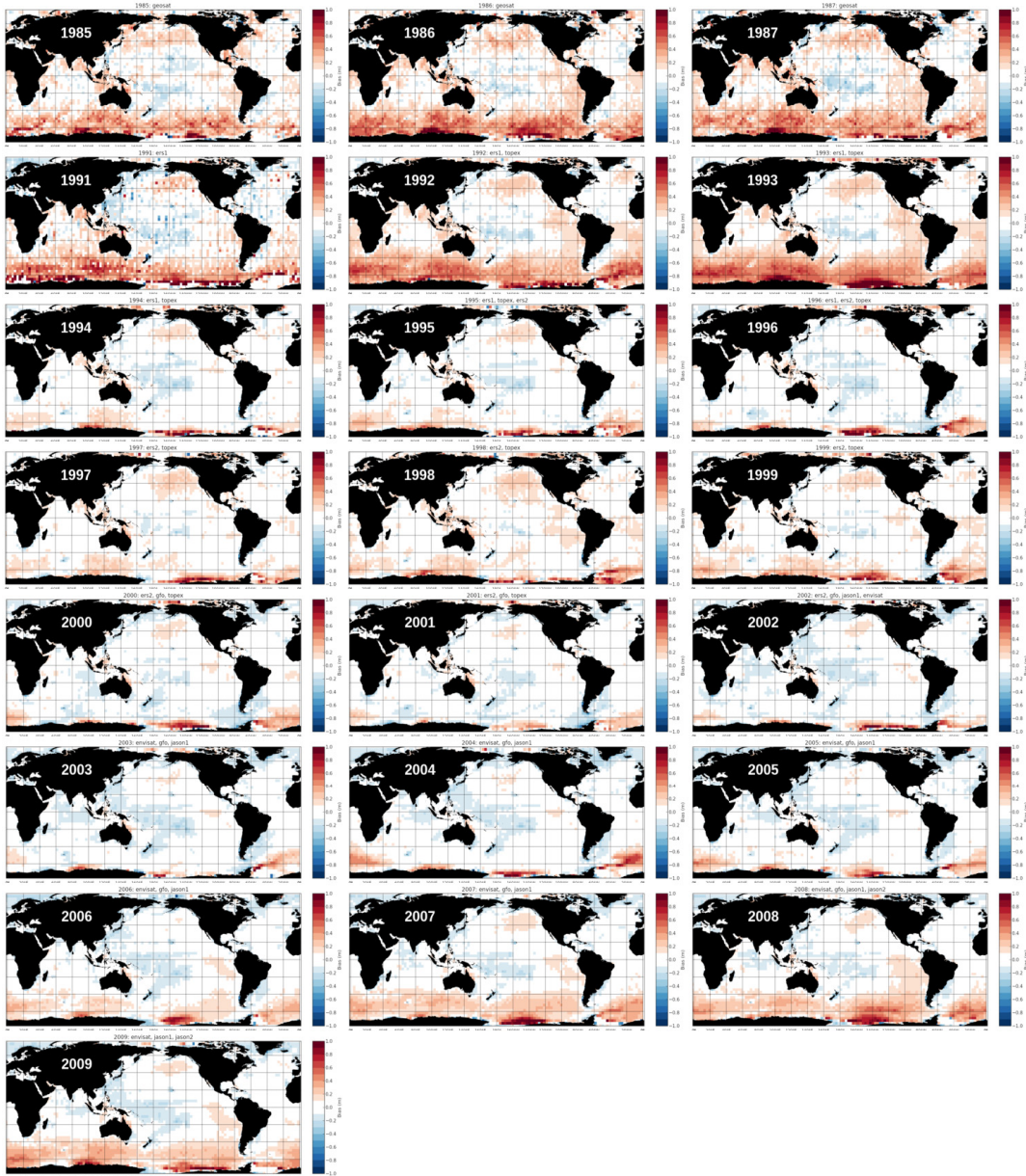


Fig. 22 H_s bias relative to altimeter data for each year for the entire altimeter record.

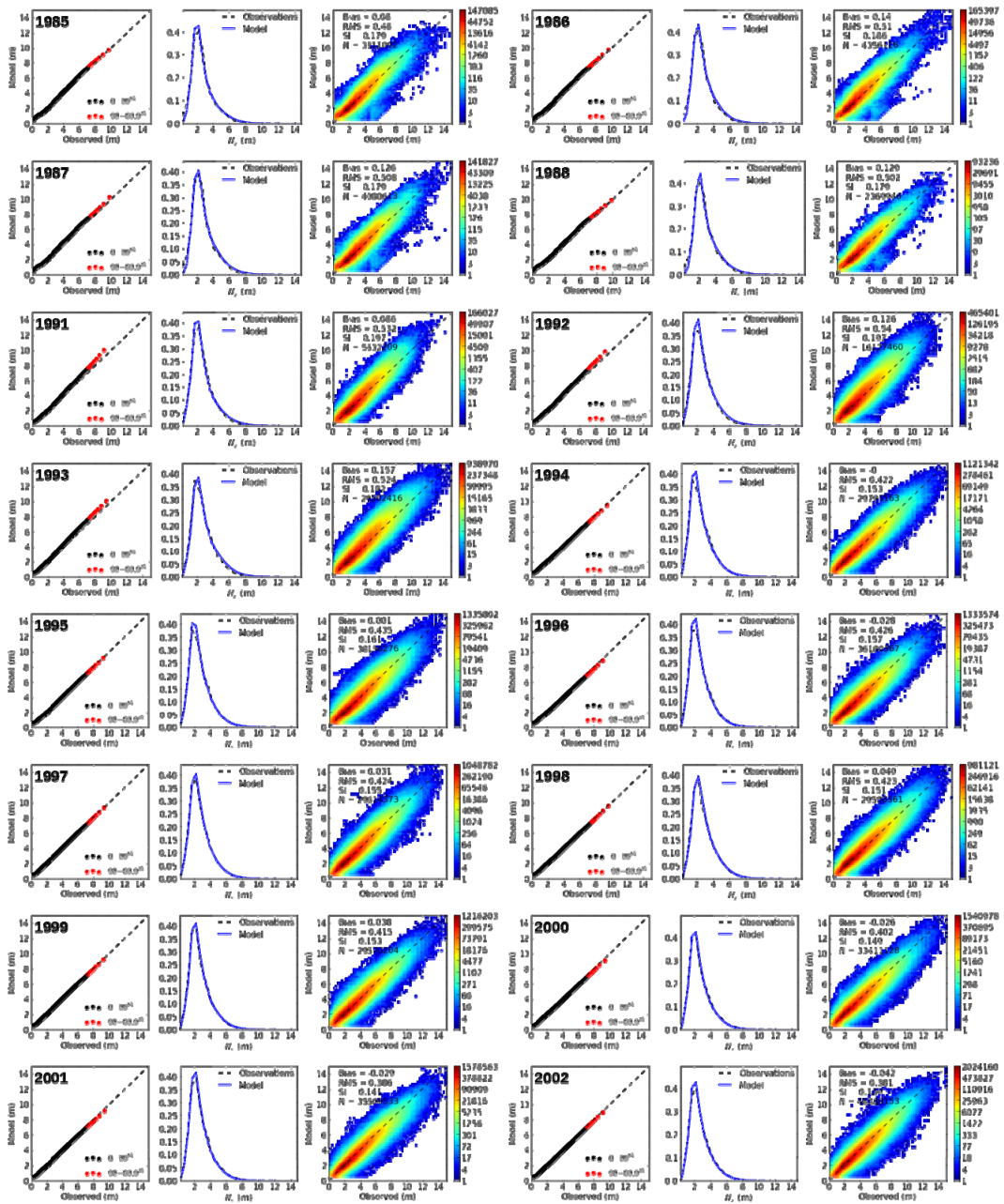


Fig. 23 QQ-plots, PDF's and scatter density plots of H_s calculated from model-altimeter co-locations separately for each year covered by the altimeter record.

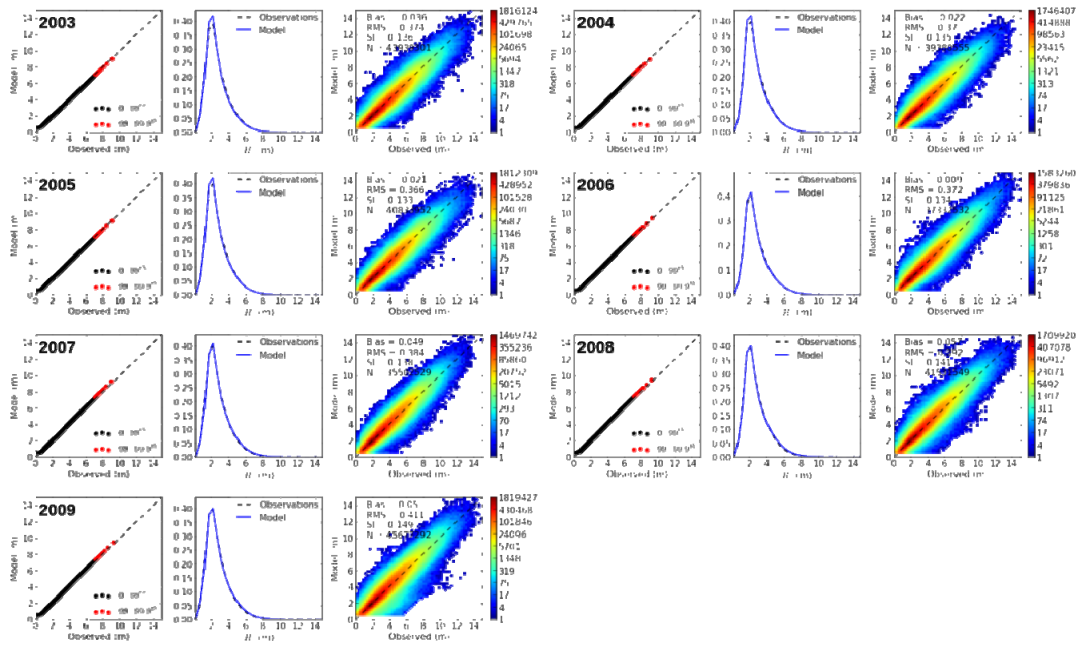


Fig.23 Continued

APPENDIX D ADDITIONAL NDBC VALIDATION RESULTS

Plots in this appendix include the availability of data from each of the NDBC buoys used in this work (Fig.24) and QQ-plots, PDF's and scatter density plots calculated from buoy-model co-locations for all available observations (Fig. 25).

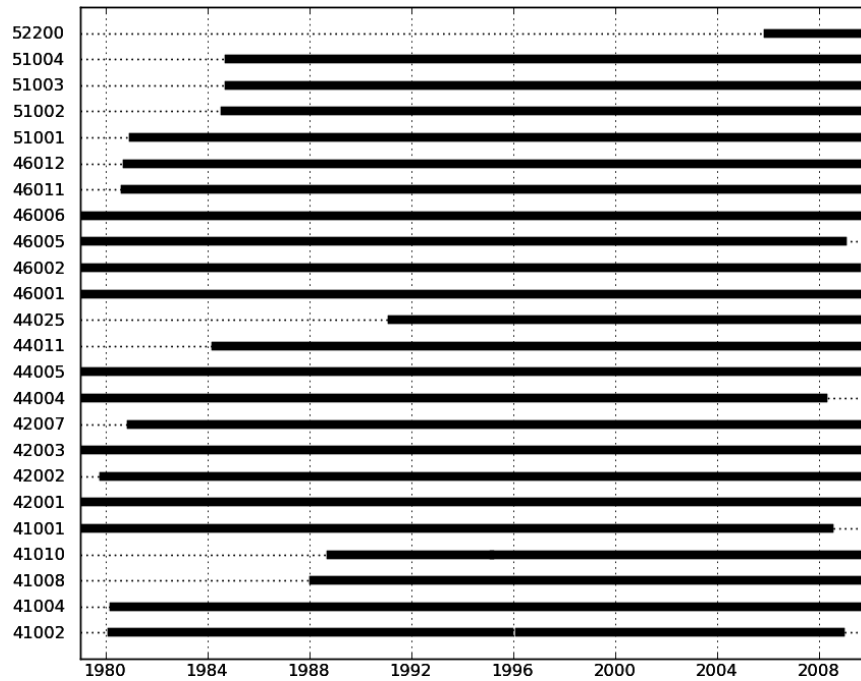


Fig. 24 Data availability for NDBC buoys used for verification

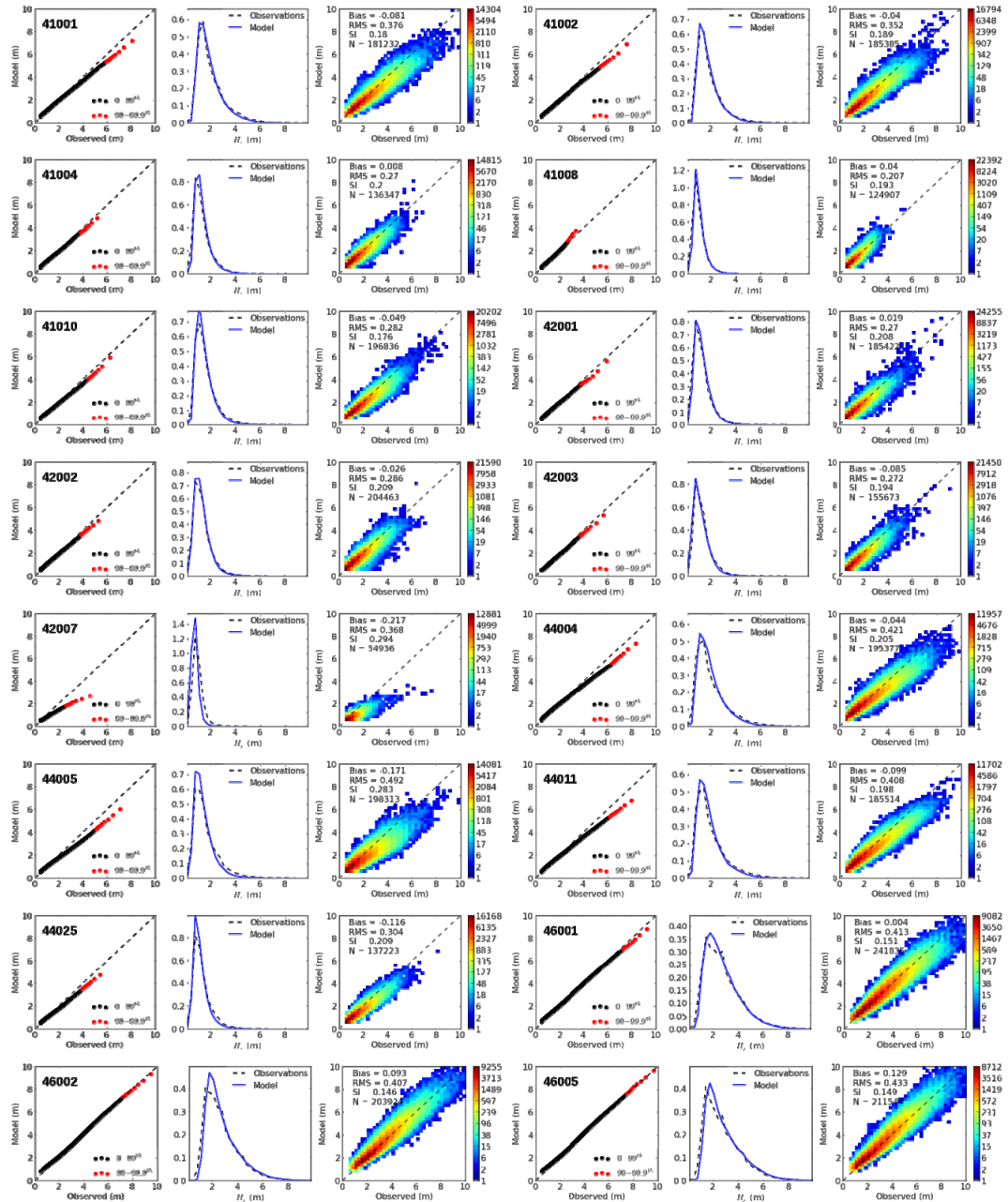


Fig. 25 Verification H_s plots for each all NDBC buoys. Plots are a quantile-quantile plot on the far left, distribution and density scatter plot

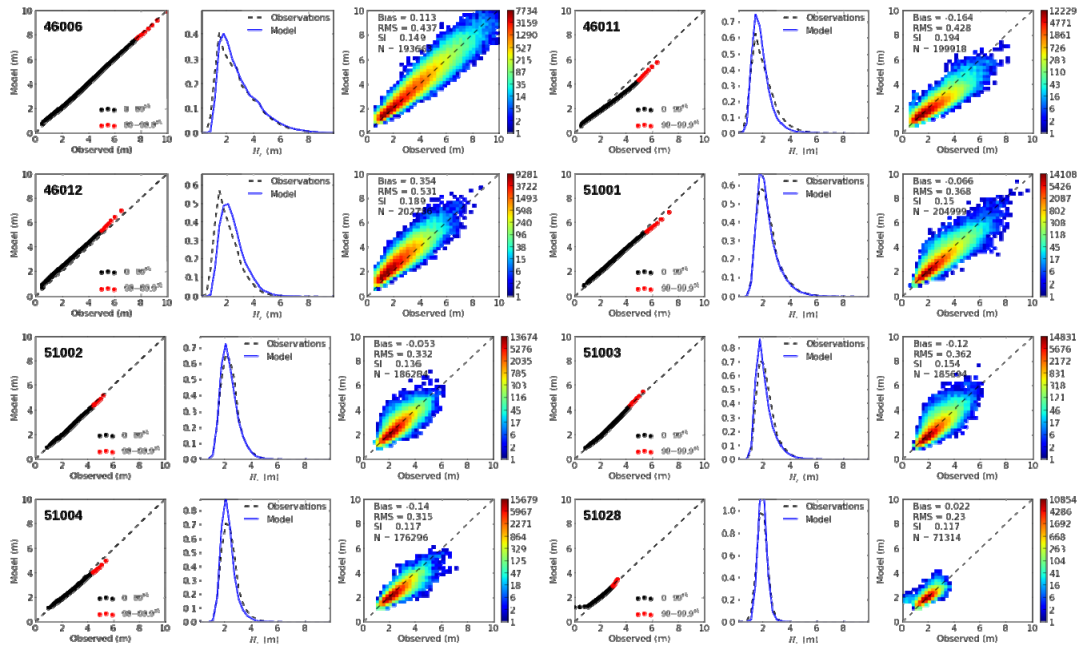


Fig. 25 Continued.

APPENDIX E ADDITIONAL SOPAC BUOY VALIDATION RESULTS

Plots in this appendix include QQ-plots, PDFs and scatter density plots and time series calculated from buoy-model co-locations for all available SOPAC buoy observations and 4° model grids (Fig. 26).

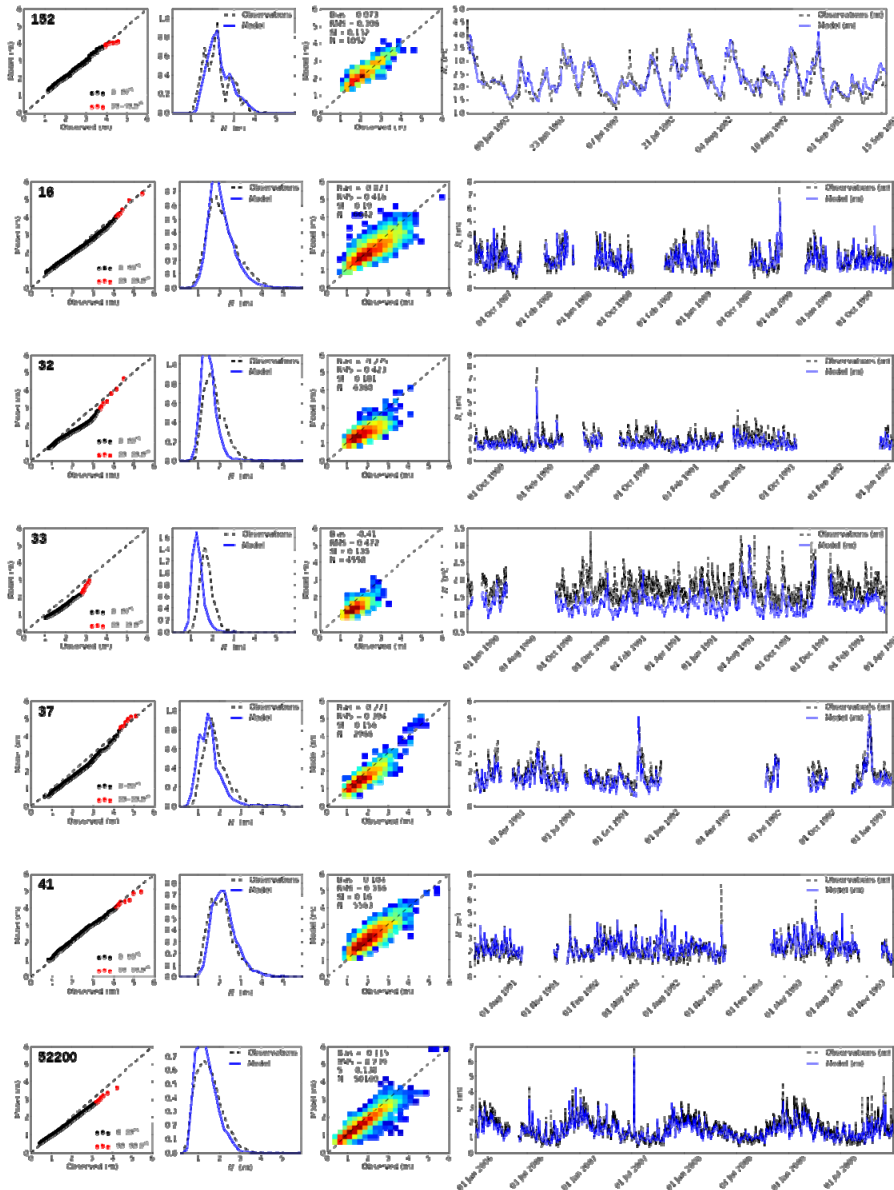
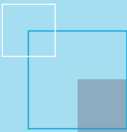


Fig. 26 H_s buoy/model QQ-plot, PDF, scatter density and time series plots for all available SOPAC buoy data.



The Centre for Australian Weather and
Climate Research is a partnership between
CSIRO and the Bureau of Meteorology.